1 Supplementary Material

1.1 Modelled Wind

Assessing the ability of the CCAM model to simulate winds over the target region is beyond the scope of this paper, but some evidence to provide confidence in the modelled meteorology is provided in this section using data from available weather stations near the measurement sites. It was not possible to attach anemometers to the top of the lighthouses where the instrumentation was housed due to the historical nature of the buildings, and the possibility of interfering with the inlet for the CRDS measurement system. Ideally eddy covariance towers located at sites away from sources of local wind distortions would be the ideal way to asses the reliability of the modelled winds. We rely on previous assessments of the CCAM at various resolutions over southern Africa to justify the use of the model to produce required meteorology for this study (Engelbrecht et al., 2009; Whittlestone et al., 2009; Engelbrecht et al., 2011; Landman et al., 2012; Engelbrecht et al., 2013, 2015)

Figure 1 presents the time series between June and September 2012 of available measured and modelled wind speeds at the Robben Island, Hangklip and Cape Point sites. At Robben Island the measured wind speed was obtained from the South African Weather Service (SAWS) Robben Island weather station, located approximately $1\,\mathrm{km}$ from the lighthouse. The modelled wind would be representative of the entire grid containing the lighthouse, and is modelled at a height of $30\,\mathrm{m}$. In general the time series plot reveals that the peaks of the observed and modelled wind speeds tend to align. The bias in the modelled data relative to the observations, is -2.7 $\mathrm{m\,s^{-1}}$, indicating that the modelled data are usually higher compared to the measurements, as expected if the winds are modelled at a greater height compared to the observations. At Hangklip measured wind speed was obtained from a weather station located approximately $2\,\mathrm{km}$ from the lighthouse, and situated more inland than the lighthouse at a height of approximately $2\,\mathrm{m}$, whereas the lighthouse is located at the edge of sea. The available data for this period show that many of the observed wind episodes are replicated by the modelled winds. The bias in the modelled winds for this period is $0.4\,\mathrm{m\,s^{-1}}$. The tower at Cape Point is equipped with an anemometer at a height of $30\,\mathrm{m}$. The time series of the measured and modelled winds show agreement, where the bias in the modelled winds is approximately $1.75\,\mathrm{m\,s^{-1}}$. The measurement tower at Cape Point is located on top of a cliff overlooking the sea, and sits at a height of approximately $238\,\mathrm{m}$ above sea level. Therefore, in terms of the height relevant to the wind, the effective height of the station is higher compared with the height of the measurement point above ground of $30\,\mathrm{m}$. This would lead to higher measured winds at the tower compared to winds modelled at $30\,\mathrm{m}$.

A plot representing the level of agreement between the measured and modelled wind speeds at the three sites is presented in Figure 2. In the plot for Robben Island, the middle horizontal line represents the bias, whereas the negative linear trend indicates that as the mean wind speed increases, the modelled wind speed tends to be larger compared to the observed wind speed, which is expected due to the height discrepancy between the observed and modelled wind speeds. The outer dashed lines represent the 95% limits if agreement, which are relatively wide in this case, extending from -8 to $7\,\mathrm{m\,s^{-1}}$. Lauvaux et al. (2016) found large variability in the differences between observed and modelled wind speeds as well, where their mismatch ranged between -5 and $8\,\mathrm{m\,s^{-1}}$. For Hangklip and Cape Point, there is no negative trend in the points, but points take on a funnel shape, indicating that the discrepancies between modelled and observed wind speeds are larger at higher wind speeds. For both of these sites, the limits of agreement are between -10 to $15\,\mathrm{m\,s^{-1}}$.

The wind direction comparison for Robben Island is presented by means of wind roses in Figures 3 and 4. The plots were produced using the openair (v2.0) package for R statistical software package (Carslaw and Ropkins, 2012). The observed wind, which was measured at the interior of the island, is dominated by winds from the south east, except in winter when this changes to the north west. The fastest winds are generally from the dominant wind direction during each season. The modelled winds also indicate that the dominant wind direction is from the south east, except in winter when it is from the north west. One notable difference is the higher frequency in wind from the west indicated by the modelled values. When wind is originating from the north through to the south east, we would expect the measurements to show enhancement from the city and industrial sources. Pollution roses plotted using the observed wind directions (Figure 5) indicate that when air originates from the north west through to the south east then concentrations of $\mathrm{CO_2}$ are higher, particularly air from the east, whereas when the air is from the west or south west, then the $\mathrm{CO_2}$ concentrations are generally below $390\,\mathrm{ppm}$ close to background levels. The pollutions roses obtained from the modelled wind directions indicate that the highest $\mathrm{CO_2}$ concentrations originate from the north west through to south east, but do also indicate some of the higher concentration air arriving from the west (Figure 6).

The lowest CO_2 concentrations are from the south. The contribution from the west occurs less than 10% of the time, but does indicate a potential discrepancy between observed and modelled data.

At Hangklip, the measurements at the local weather station are shown to be either from the north west or from the north east to south east during the autumn and winter months (Figure 7). The modelled wind at the lighthouse is dominated by winds from the south in autumn or from the north west in the winter months (Figure 8). Discrepancies could be due to the local topography differences between the two locations. Concentrations of CO_2 were generally lower compared with those at Robben Island. The pollution rose for the observed wind directions show that higher concentrations of CO_2 were observed when the wind was from the north west to north east (Figure 9). Some high values also occurred when the wind was observed from the south east, which we would expect to be quite clean. The modelled wind pollution roses indicate that when wind was from the north to north east, higher CO_2 concentrations were observed in autumn, and in winter it shows higher values of CO_2 concentrations when the wind was from the south west (Figure 10). This could be when air was originating from the False Bay region.

The observed winds at Cape Point indicate that in autumn winds predominately came from the east or south east (Figure 11). In spring and summer these wind directions were very dominant, with some wind occurring from the north west in spring. In winter the wind direction was mainly from the north west. The modelled winds show wind direction during autumn was dominated by south easterly winds (Figure 12). In spring the modelled winds show dominance from the north west, whereas in summer the winds were mainly modelled to be from the south east. In winter the winds were modelled again to be from the north west, which agrees with the observed winds. CO_2 concentrations at the Cape Point site were predominantly lower (between 385 and 395 ppm) compared with Robben Island and Hangklip (Figure 13). When concentrations were high, the winds were observed to be from the north west or east, but this is less clear for the winter months. Modelled winds showed higher concentrations of CO_2 when wind was from the north west or south east. Cape Town is located to the north east of Cape Point, but wind very rarely originated from this direction, and therefore the elevated CO_2 concentrations we would expect to see from air originating from Cape Town does not appear in the plots.

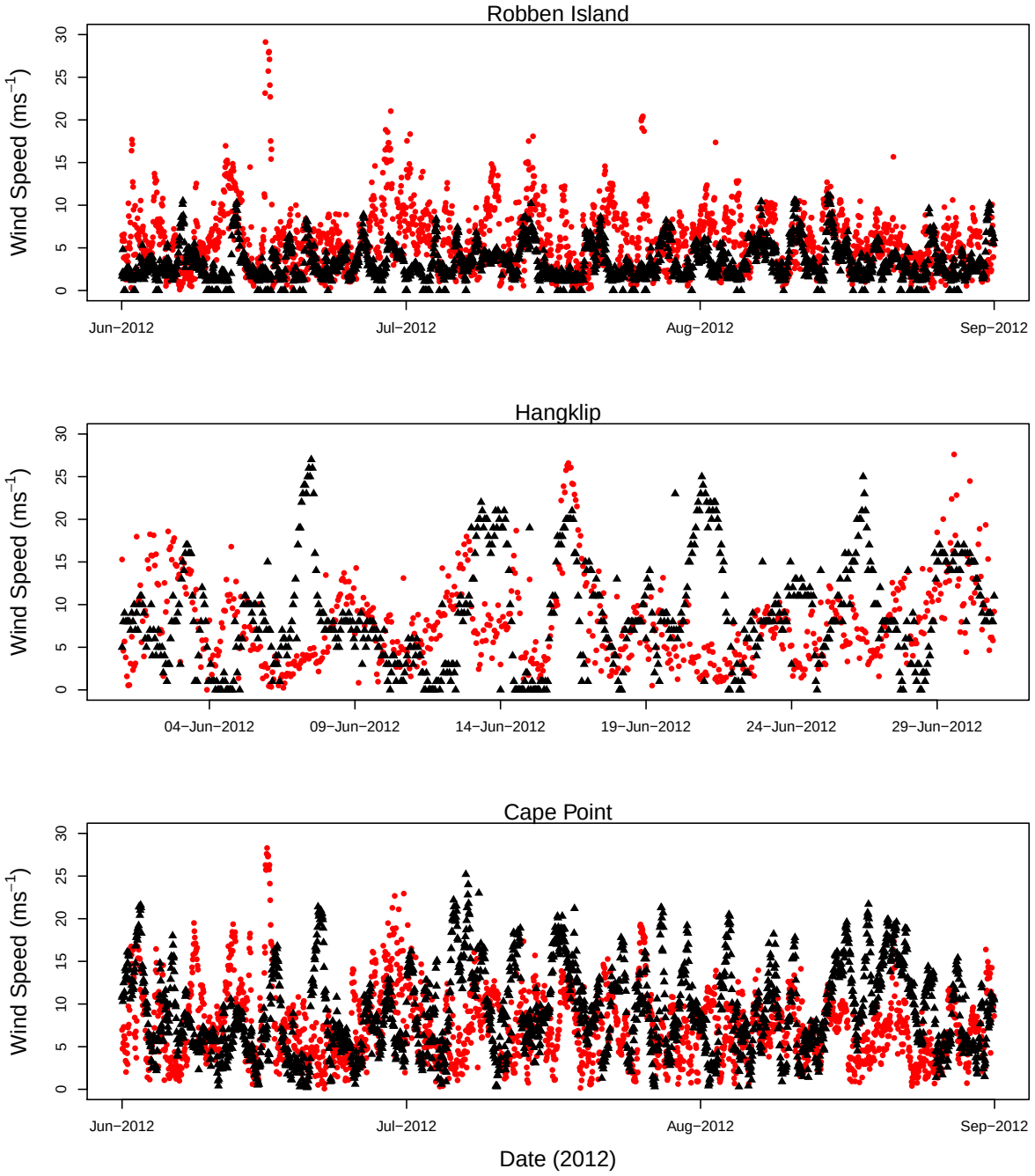

Figure 1. Time series plots of measured (triangles) versus modelled (circles) wind speed ($\mathrm{m\,s^{-1}}$) in winter 2012. The wind speeds were modelled by the regional climate model CCAM at a spatial resolution of resolution of $1\,\mathrm{km}$ by $1\,\mathrm{km}$, and the wind vectors extracted at a height of $30\,\mathrm{m}$ at each measurement location.

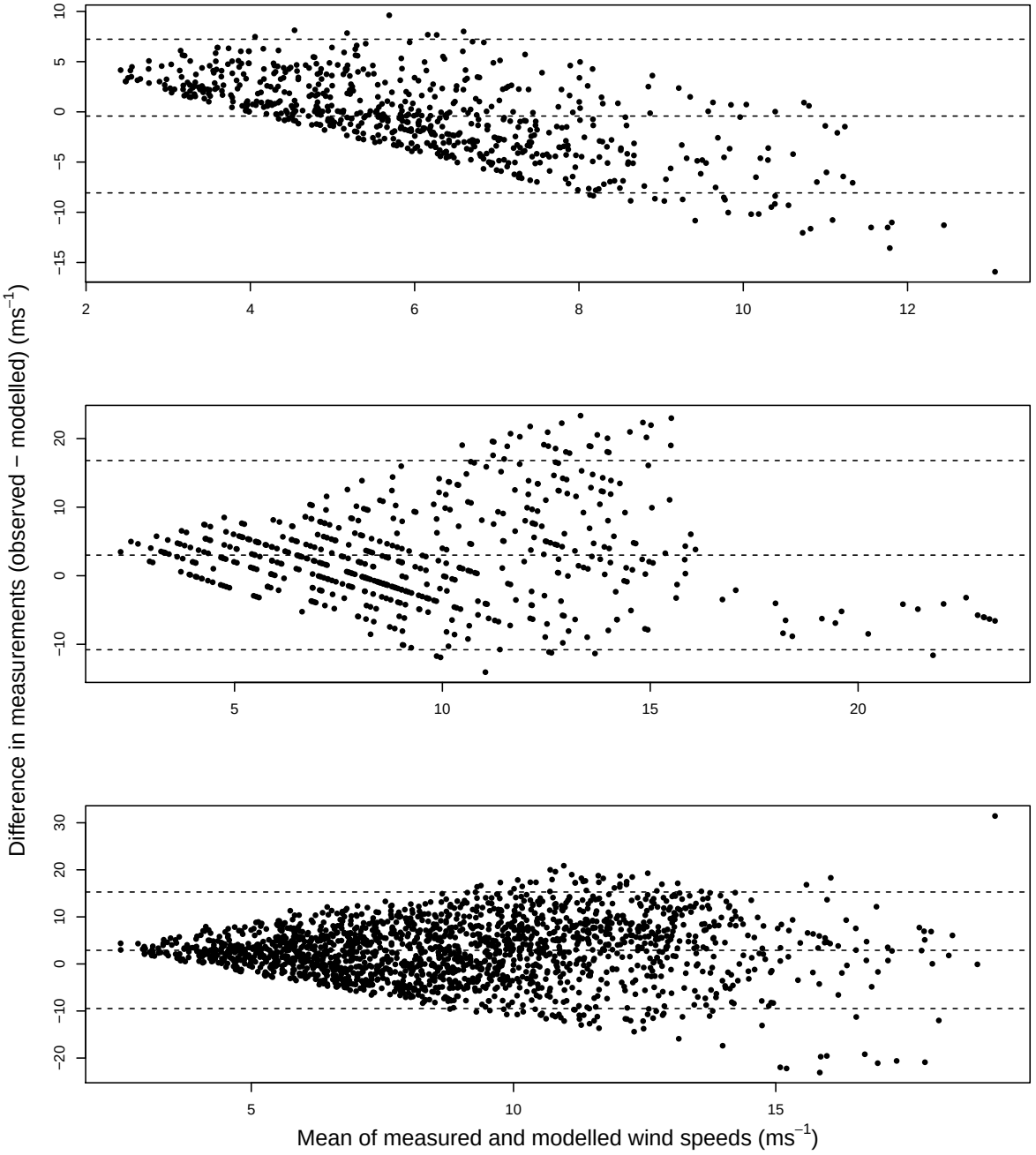

Figure 2. Bland Altman plot to show level of agreement between measured versus modelled wind speed at the Robben Island site during winter 2012, when measured wind speed is above $4\,\mathrm{m\,s^{-1}}$. The middle dashed line represents the mean bias and the outer lines the 95% limits of agreement, which represents the range between which 95% of the differences were located.

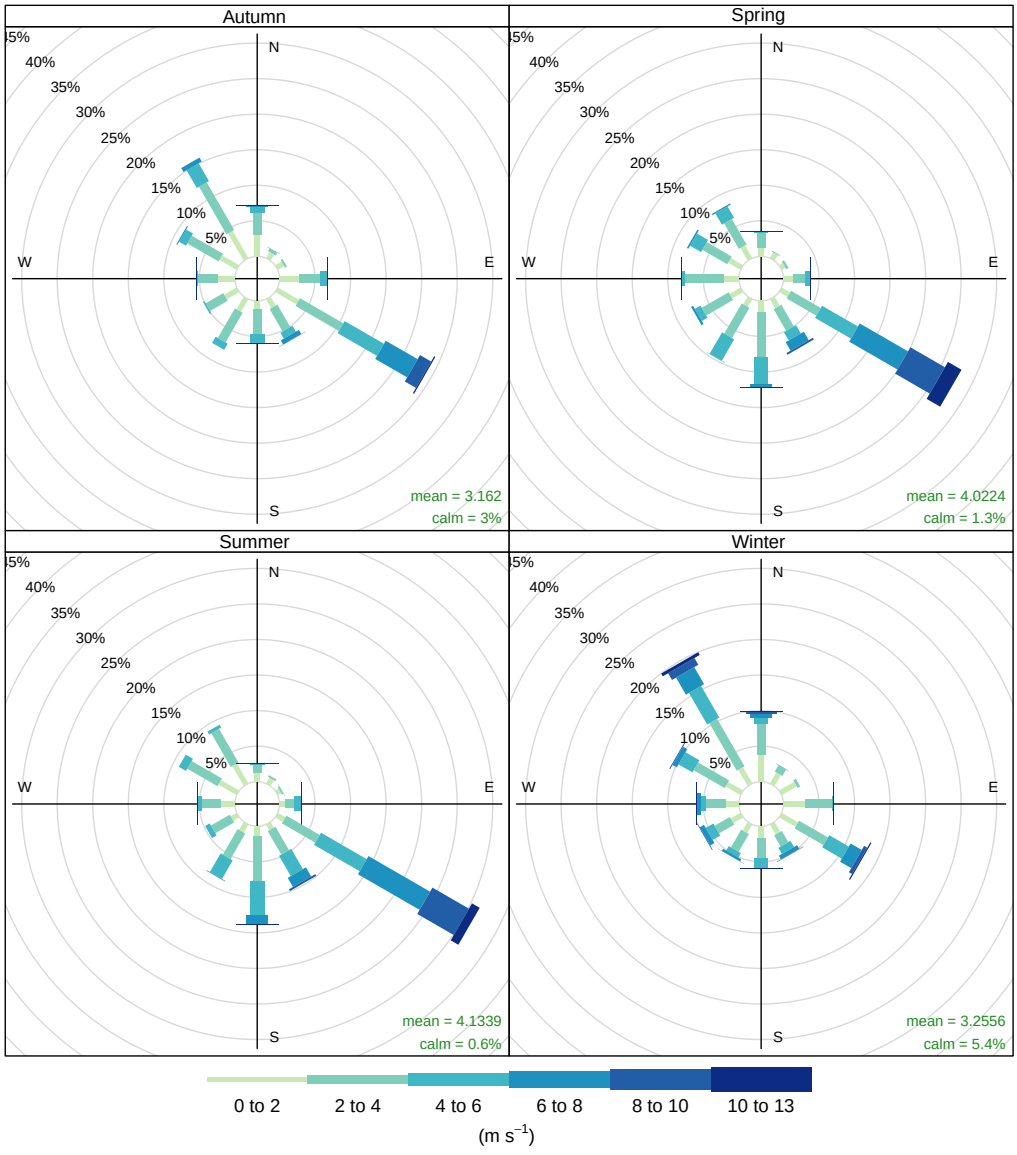

Figure 3. Wind roses showing the dominant wind directions at Robben Island for each season, as measured at 2 m at the Robben Island SAWS weather station.

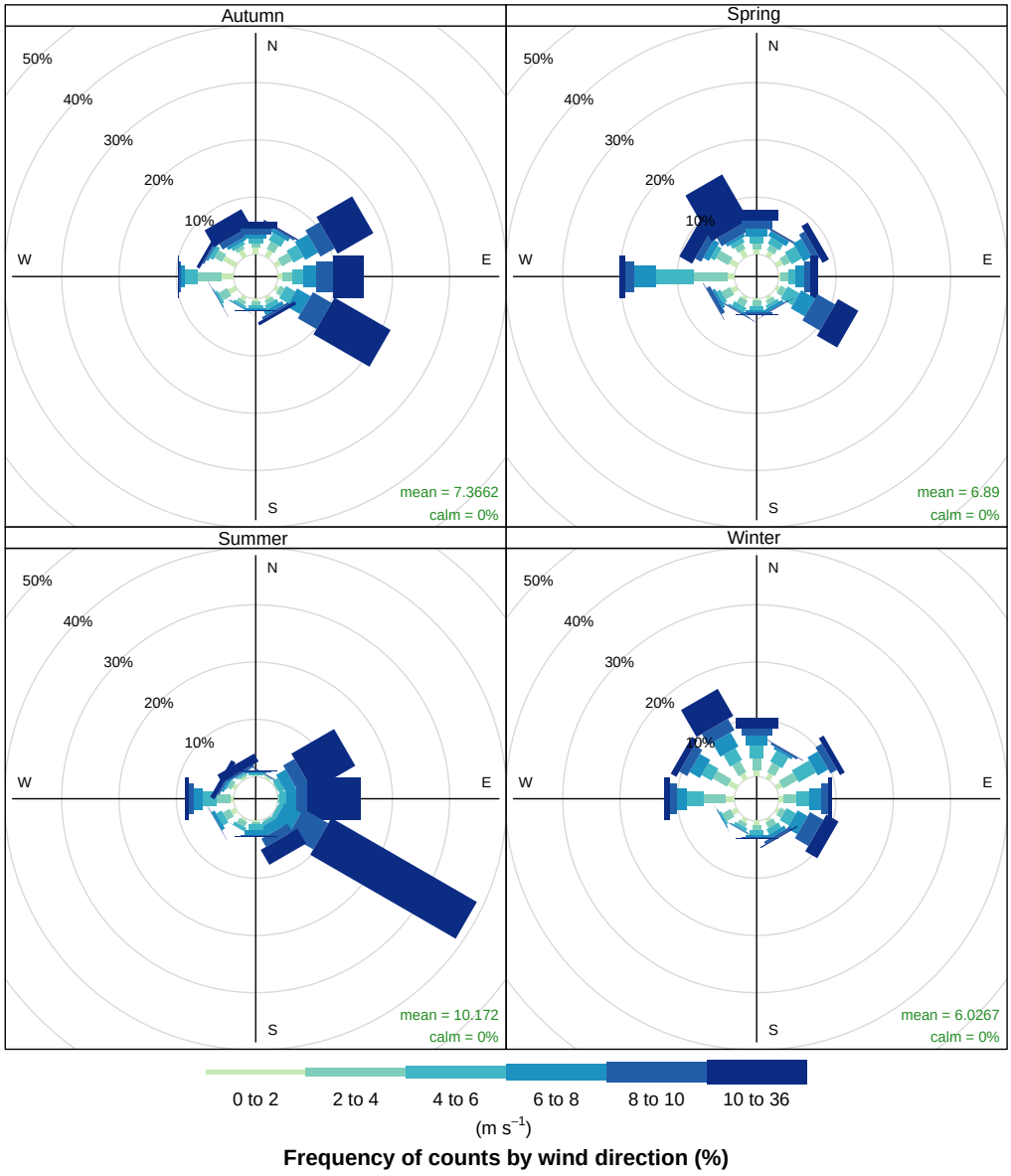

Figure 4. Wind roses showing the dominant wind directions at Robben Island for each season, as modelled at 30 m at the Robben Island lighthouse.

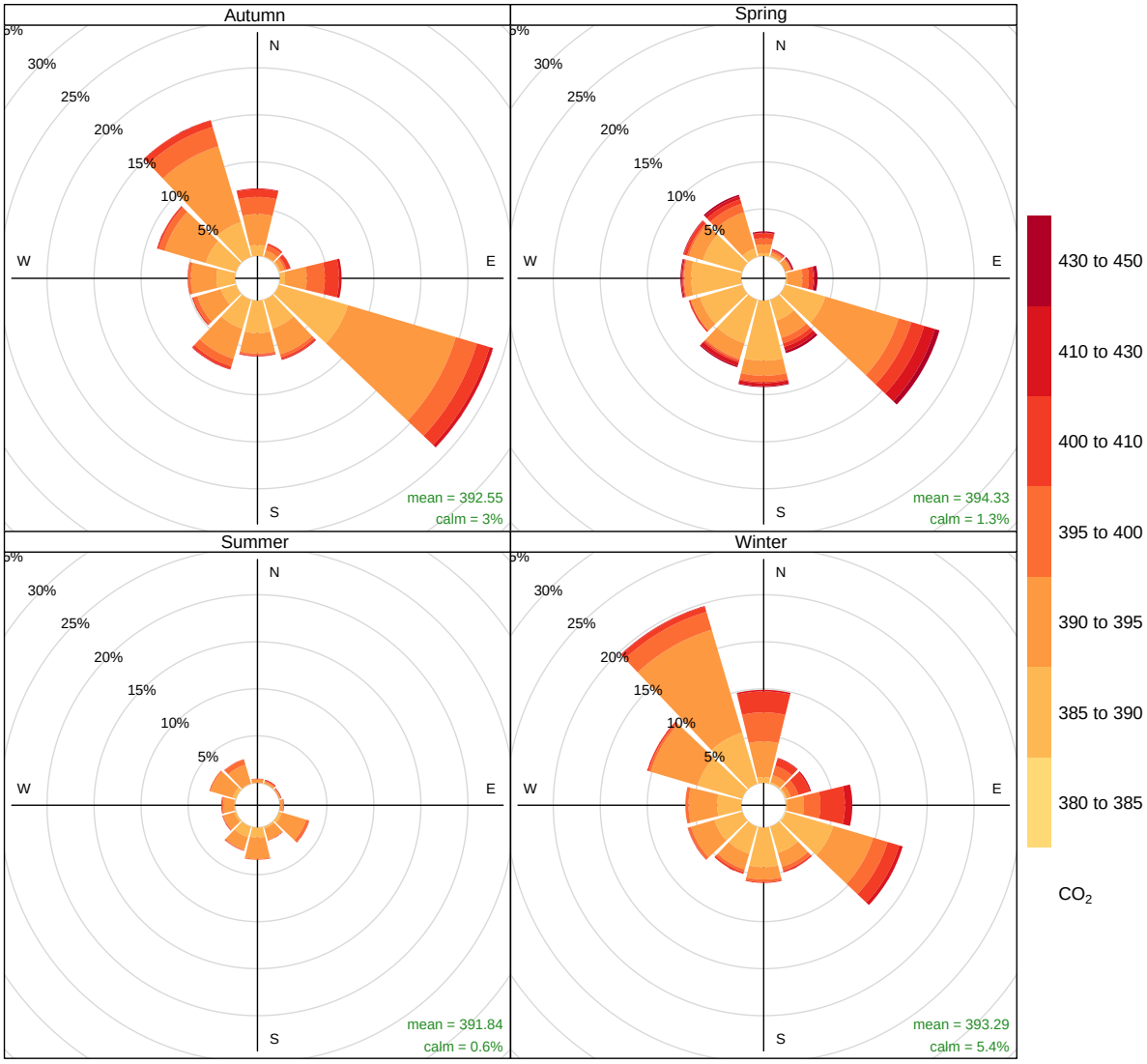

Figure 5. Pollution rose for CO_2 (ppm) for Robben Island showing the concentration distribution for each wind direction as observed at the Robben Island SAWS weather station.

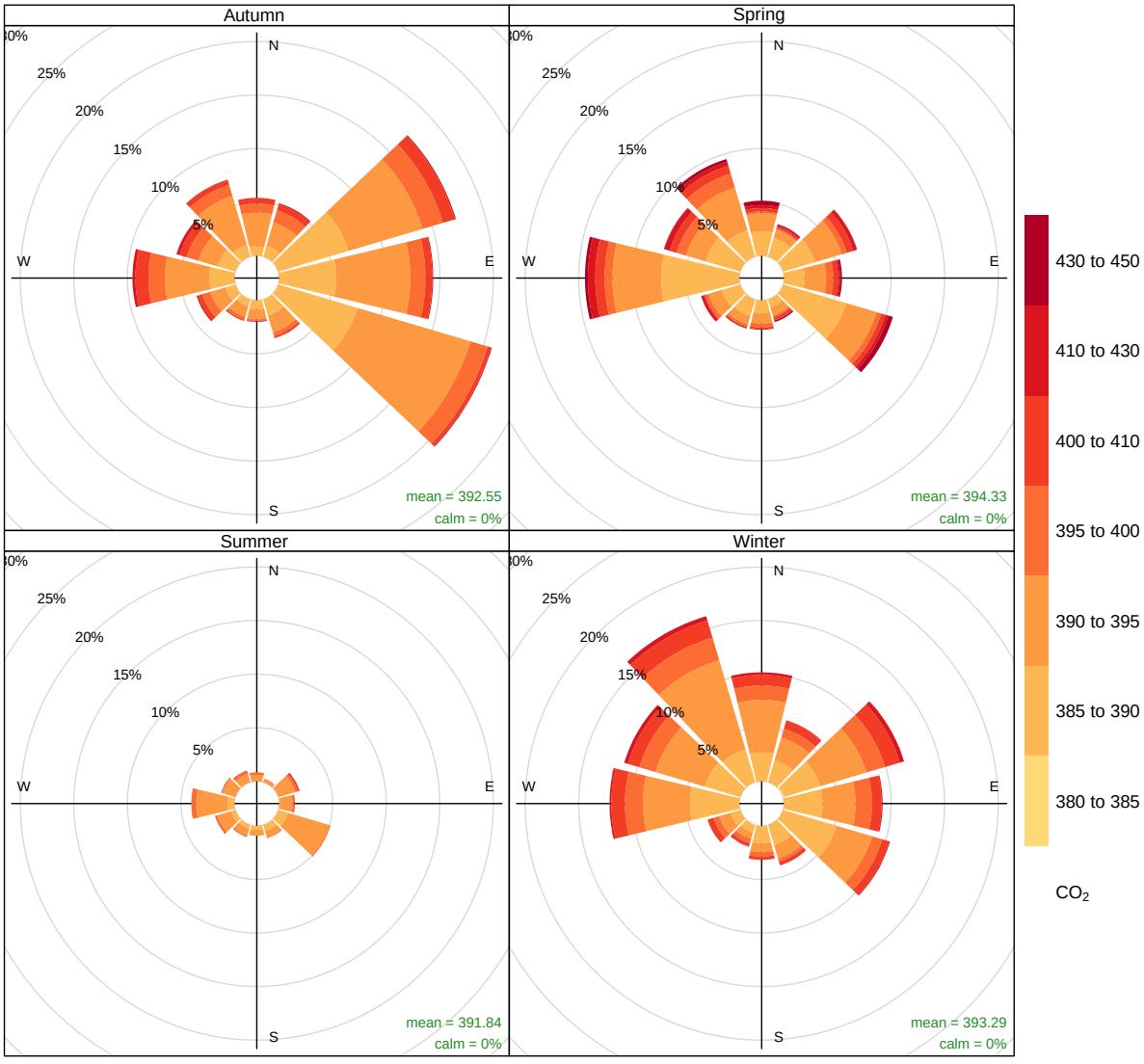

Figure 6. Pollution rose for CO_2 (ppm) for Robben Island showing the concentration distribution for each wind direction as modelled by CCAM at a height of 30 m for the grid containing the Robben Island lighthouse.

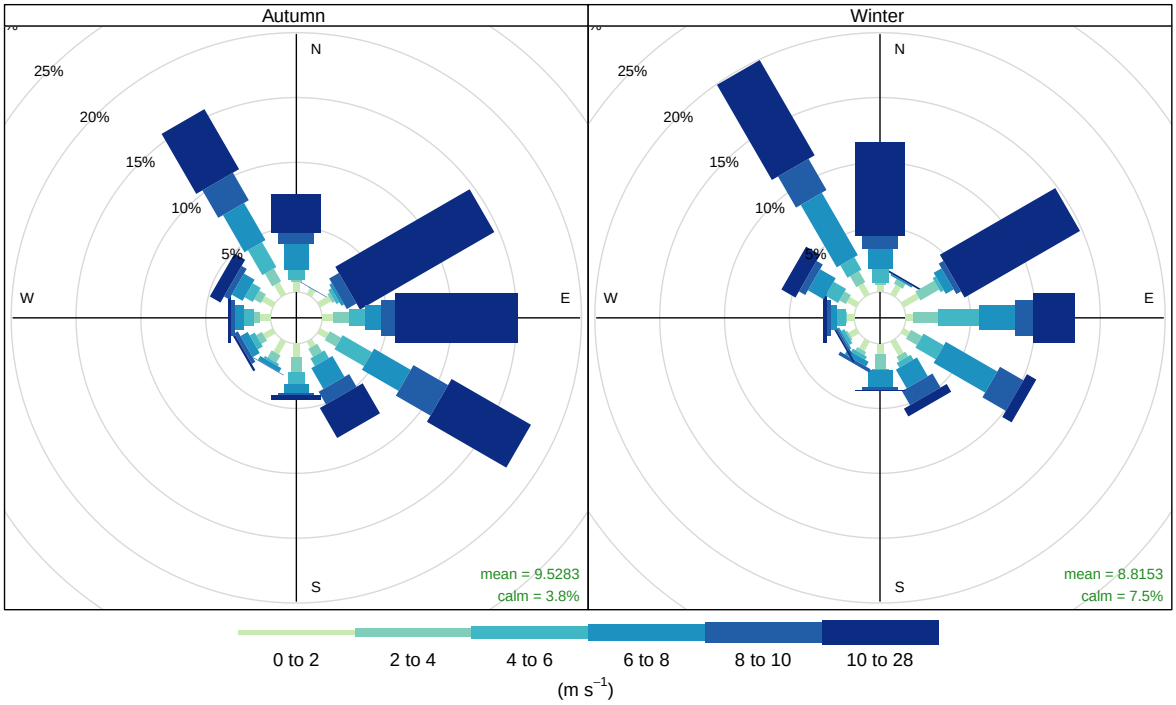

Figure 7. Wind roses showing the dominant wind directions at Hangklip for each season, as measured at 2 m at the weather station approximately 2 km from the lighthouse.

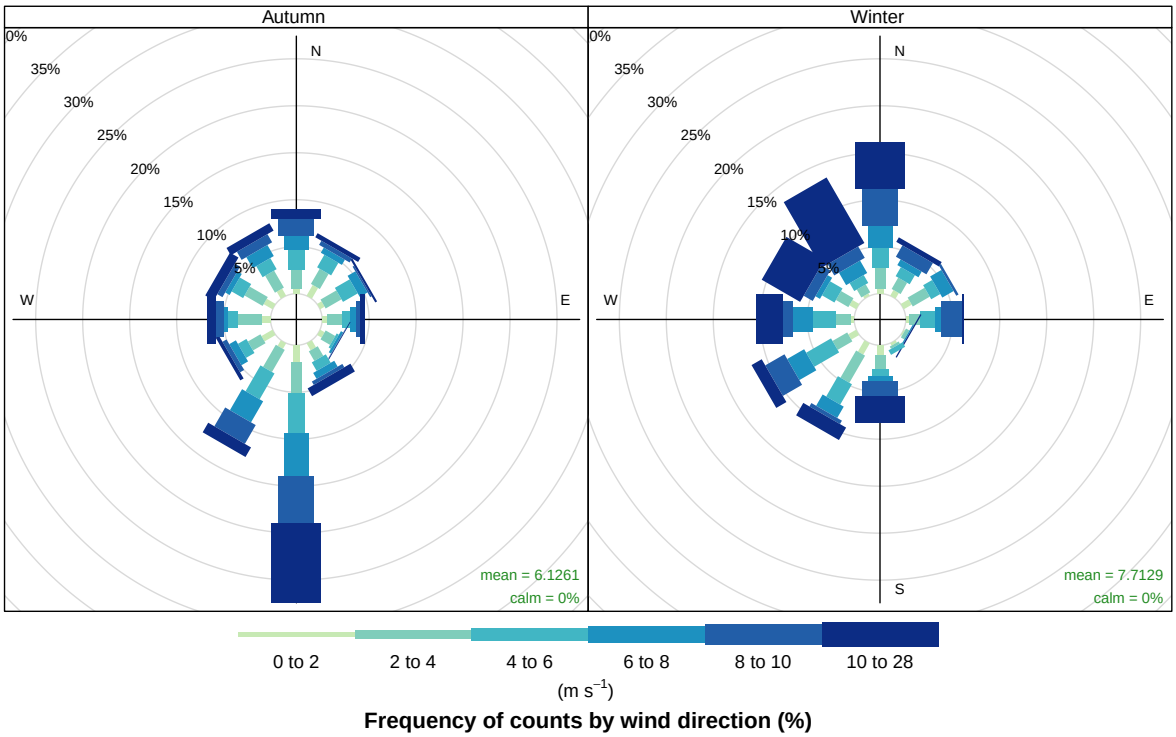

Figure 8. Wind roses showing the dominant wind directions at Hangklip for each season, as modelled at 30 m at the Hangklip lighthouse.

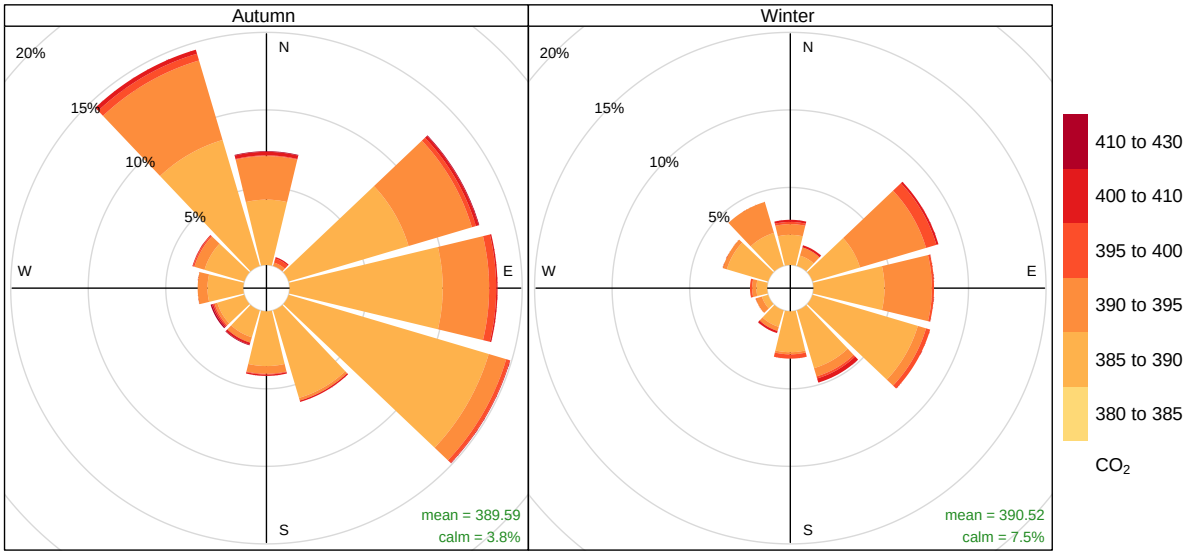

Figure 9. Pollution rose for CO_2 (ppm) for Hangklip showing the concentration distribution for each wind direction as observed at the Hangklip local weather station.

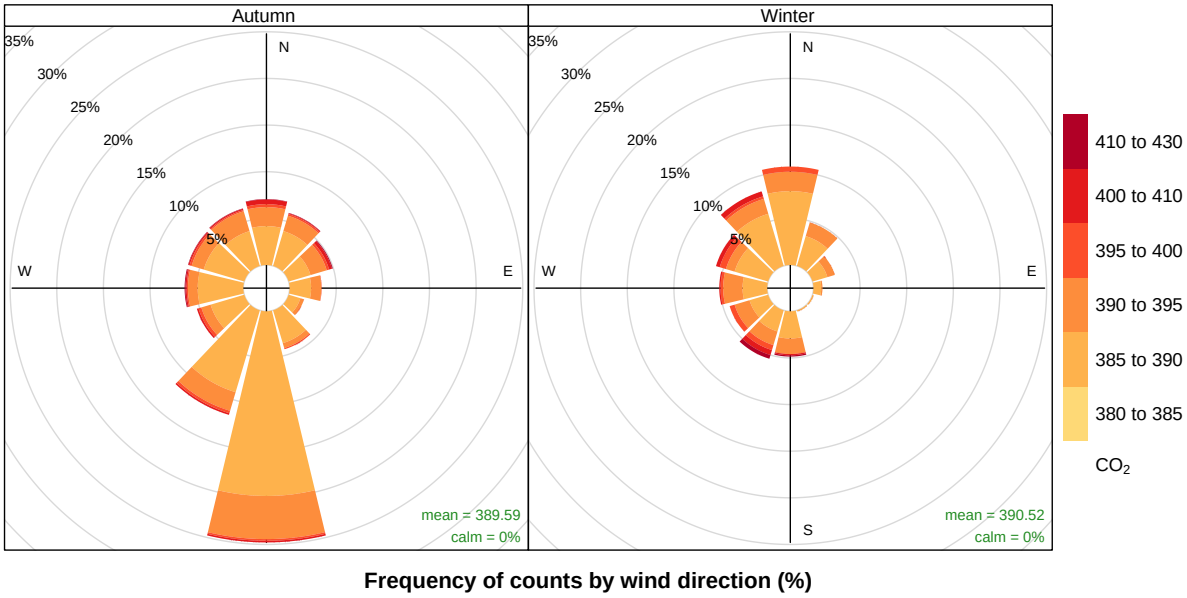

Figure 10. Pollution rose for CO_2 (ppm) for Hangklip showing the concentration distribution for each wind direction as modelled by CCAM at a height of 30 m for the grid containing the Hangklip lighthouse.

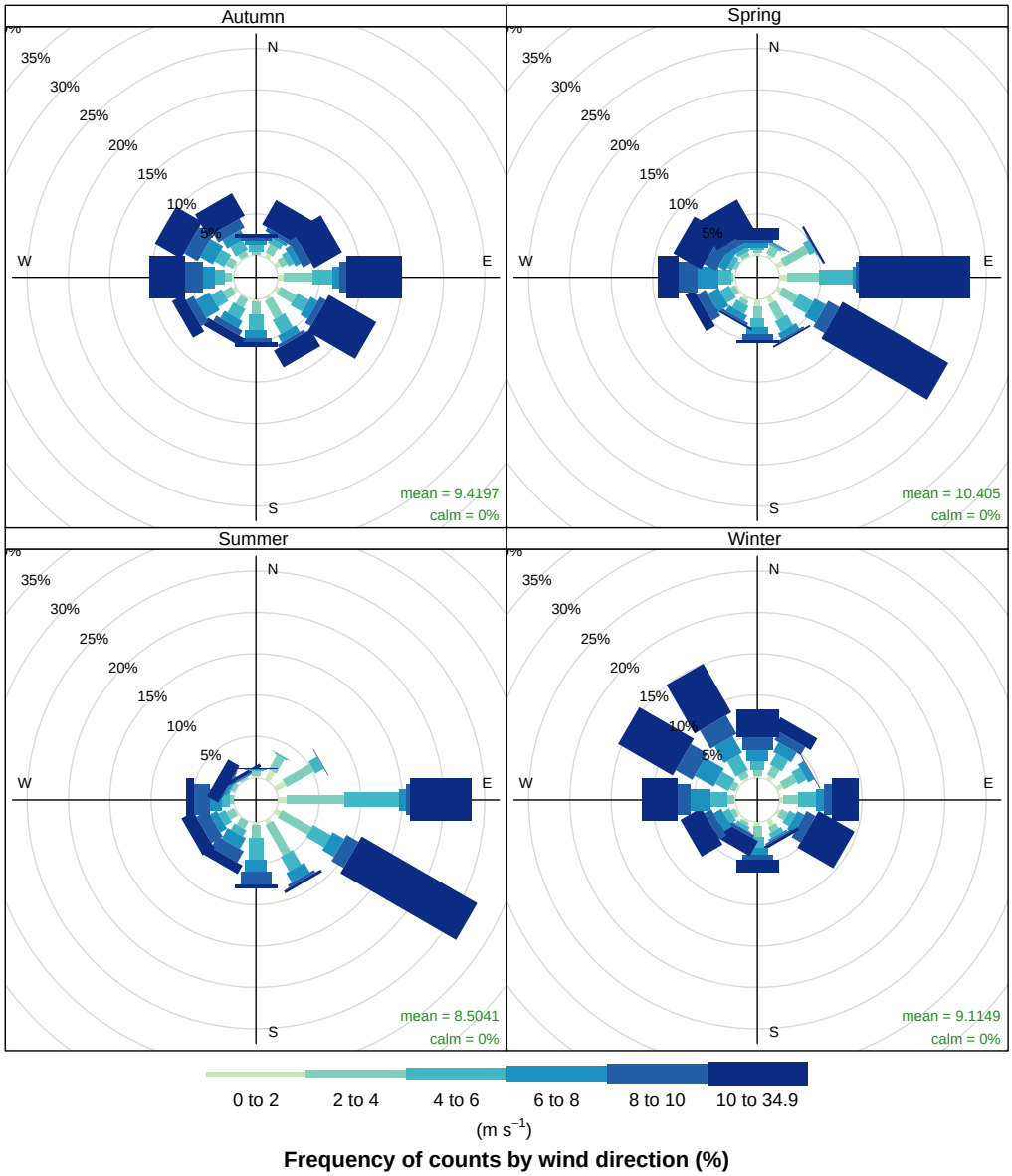

Figure 11. Wind roses showing the dominant wind directions at Cape Point GAW station for each season, as measured at 30 m on the measurement tower.

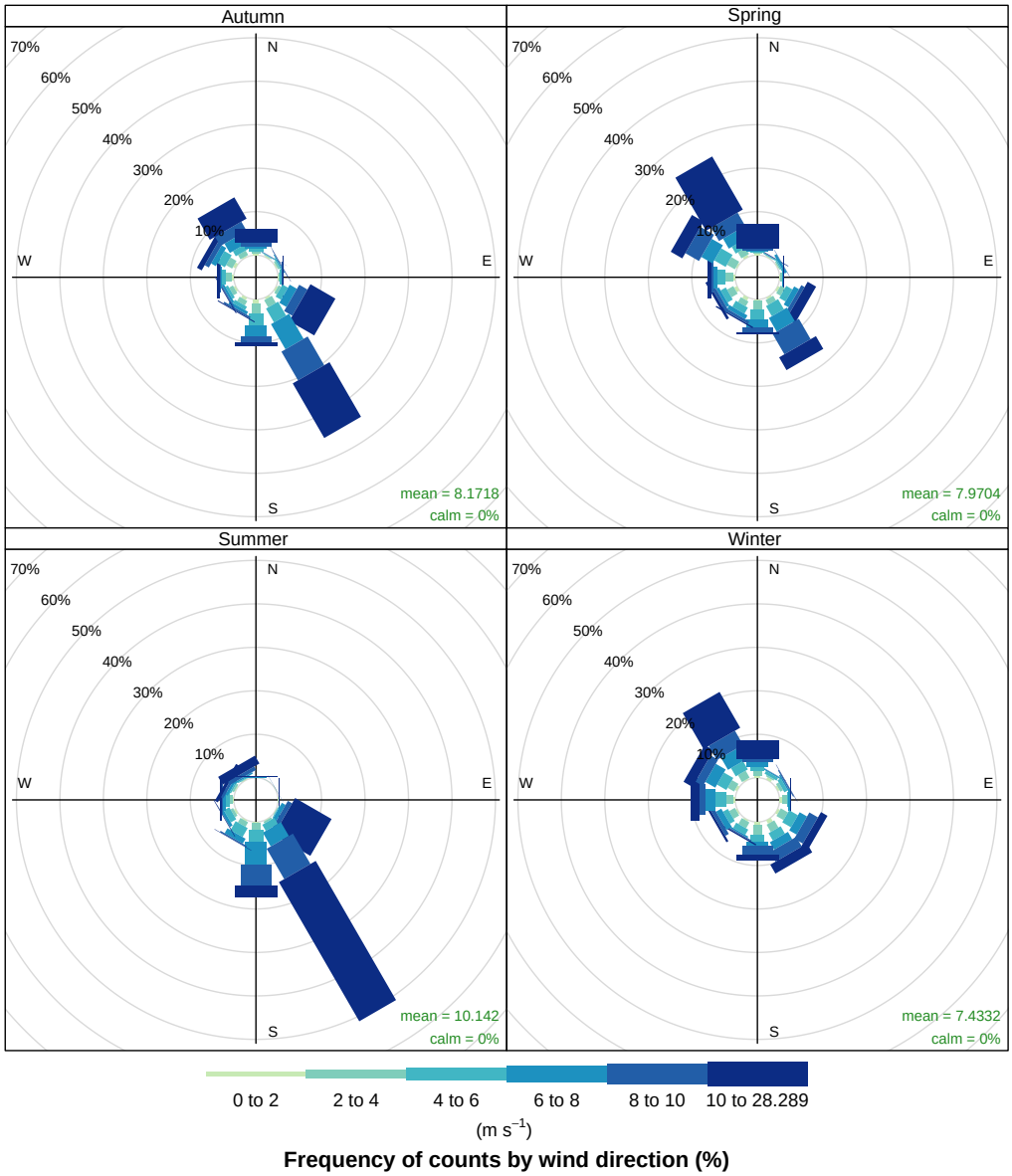

Figure 12. Wind roses showing the dominant wind directions at Cape Point GAW station for each season, as modelled at 30 m at the Cape Point GAW station.

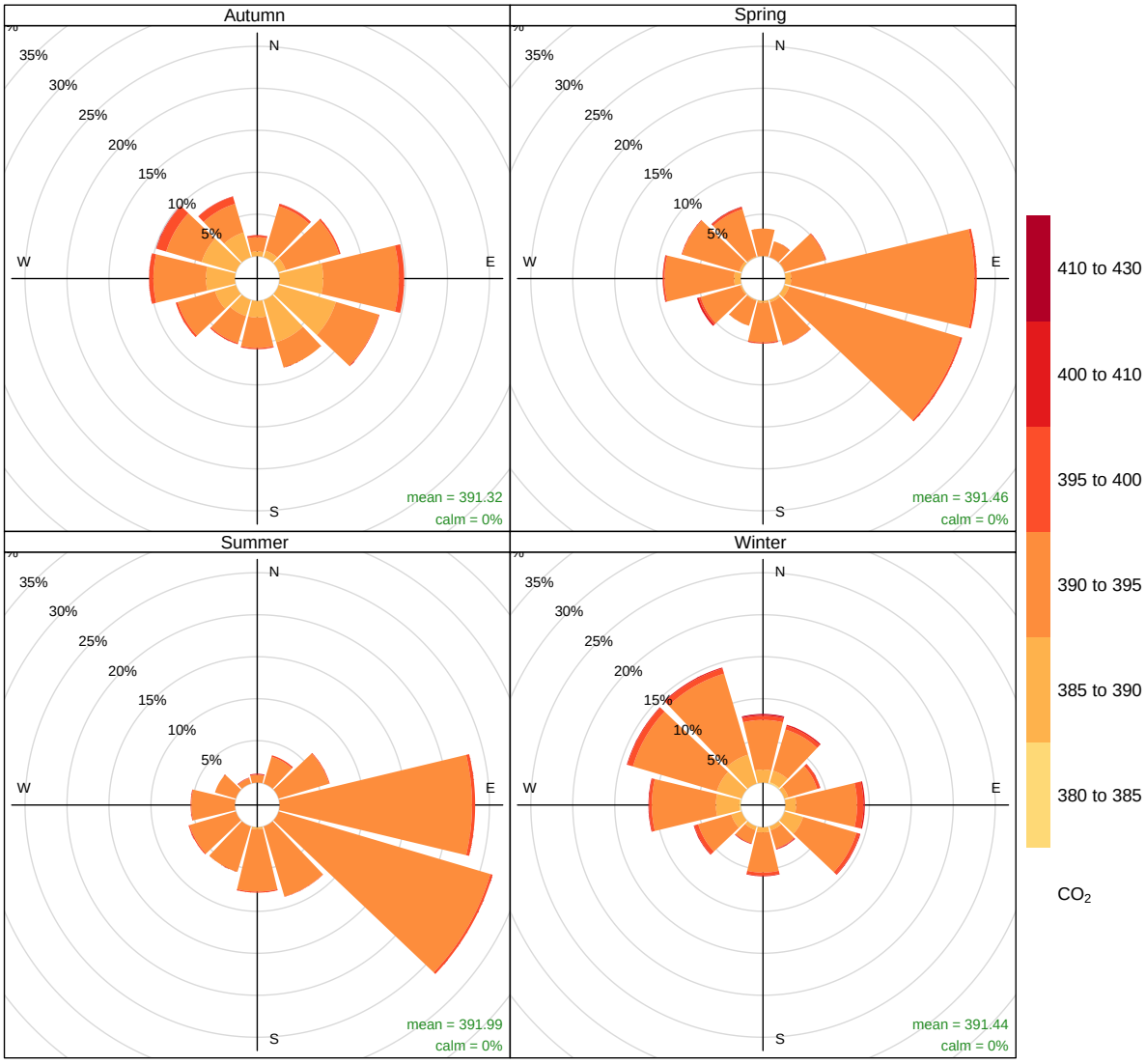

Figure 13. Pollution rose for CO_2 (ppm) for Cape Point GAW station showing the concentration distribution for each wind direction as observed at the Cape Point GAW station.

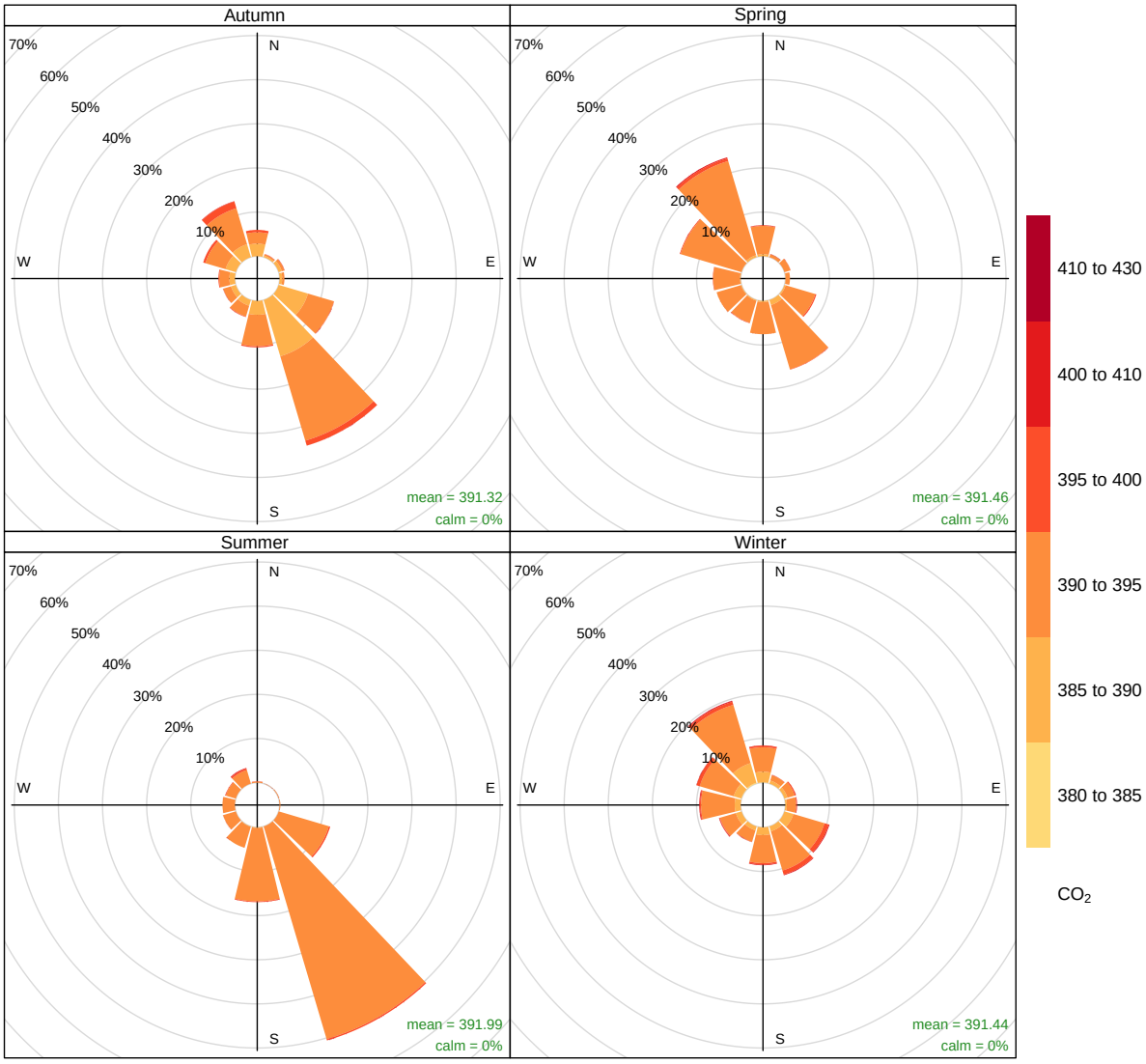

Figure 14. Pollution rose for CO_2 (ppm) for Cape Point GAW station showing the concentration distribution for each wind direction as modelled by CCAM at a height of 30 m for the grid containing the Cape Point GAW station.

1.2 Diurnal Cycle

The observed, prior and posterior modelled diurnal cycle, separated into working week and weekend CO_2 concentrations, are provided for each site and for each month in Figures 15 and 16. For all months, the diurnal cycle of the posterior modelled concentrations is relatively flat in comparison with the observed diurnal cycle, and usually sits at a higher mean level in the case of Robben Island, and at a lower mean level in the case of Hangklip. Compared to the prior modelled concentrations, the posterior diurnal cycle matches better with the observed concentrations in terms of the peaks and troughs of the cycle and in terms of the mean level of the concentrations at each hour, although the posterior cycle still appears relatively flat in comparison to the observed cycle.

April 2013 at the Robben Island site provides an example where the prior modelled concentrations had working week concentrations that were above those for the weekend during the early morning hours, whereas the observed concentrations showed the opposite situation. After the inversion, the posterior estimates had mean concentrations for the weekend that were above those for the working week during the early morning hours, matching better with the observed diurnal cycle.

Therefore the inversion does show an ability to improve estimates of the diurnal cycle, despite only separating the sources into day and night sources over a week period, and further separating the fossil fuel sources into weekend and week sources.

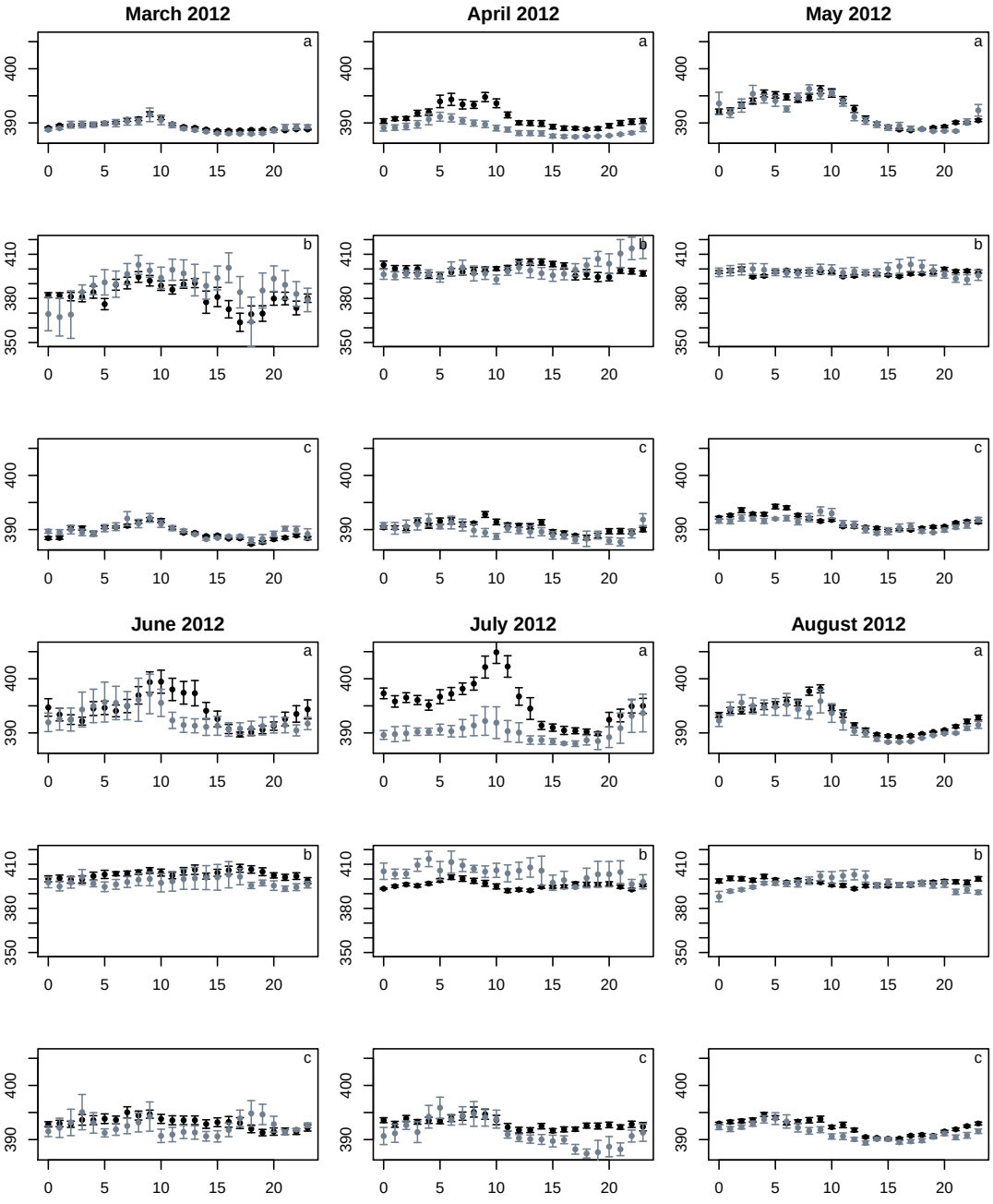
March 2012
April 2012
May 2012
June 2012
July 2012
August 2012
a
b
c
390
400
350
380
410
0
5
10
15
20

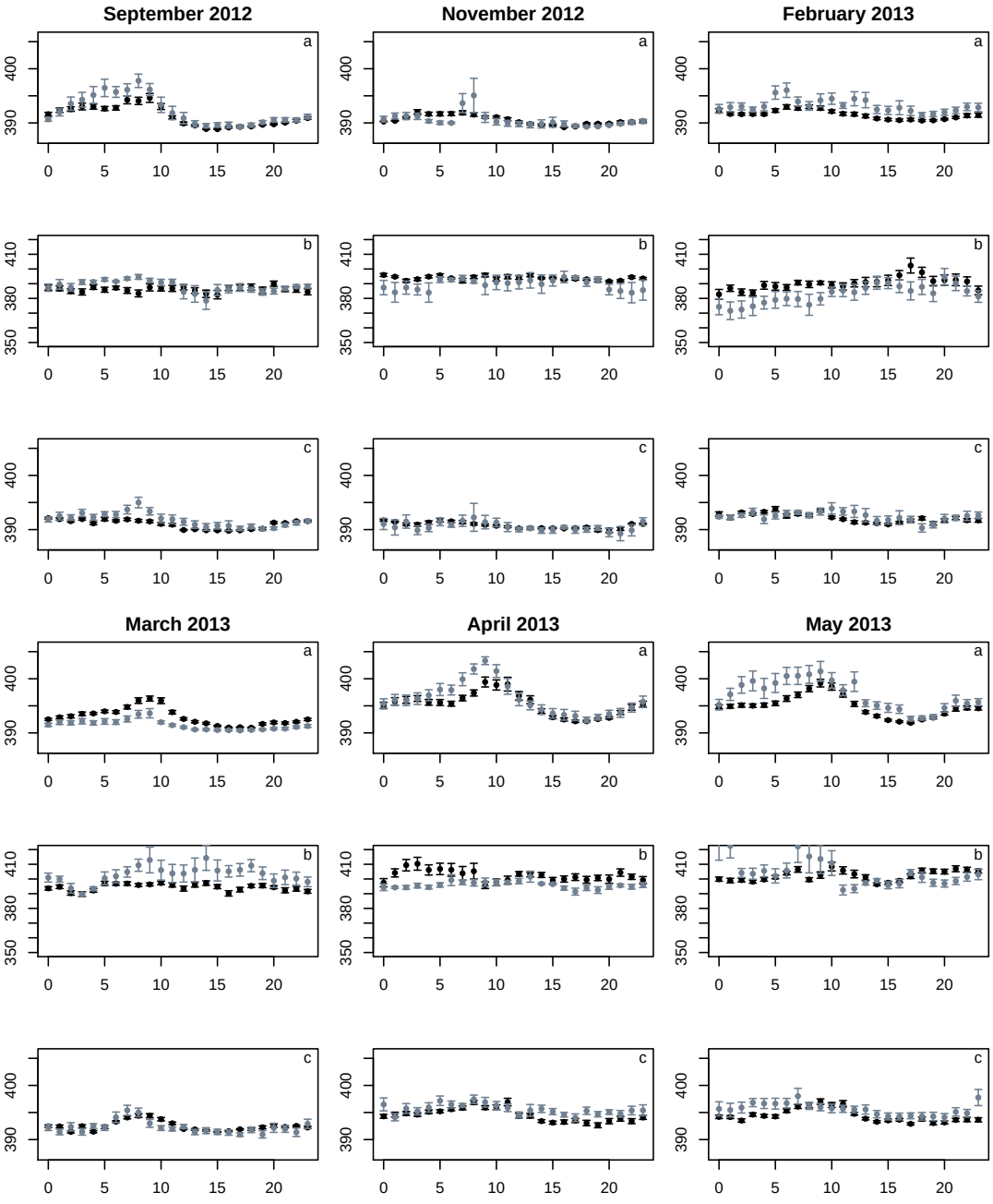
September 2012
November 2012
February 2013
March 2013
April 2013
May 2013
a
b
c
0 5 10 15 20
390 400
350 380 410

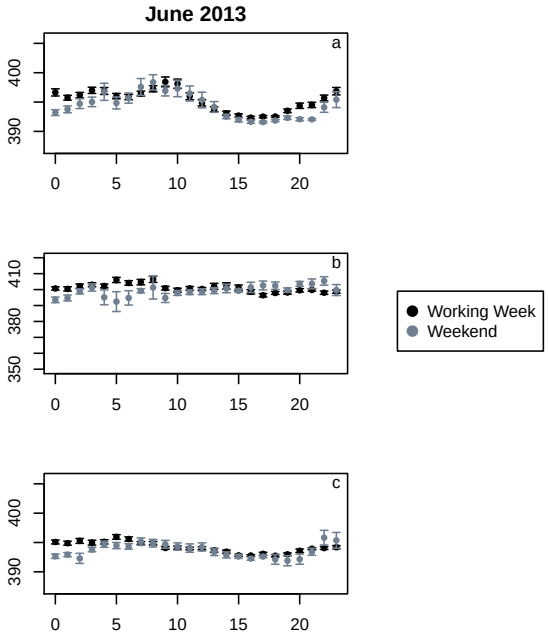

Figure 15. Diurnal cycle of the observed CO_2 concentrations (ppm) at Robben Island, separated into working week (black) and weekend concentrations (grey), for each month with standard error bars, where the standard error is calculated over all measurements available for that hour of the day during that particular month.

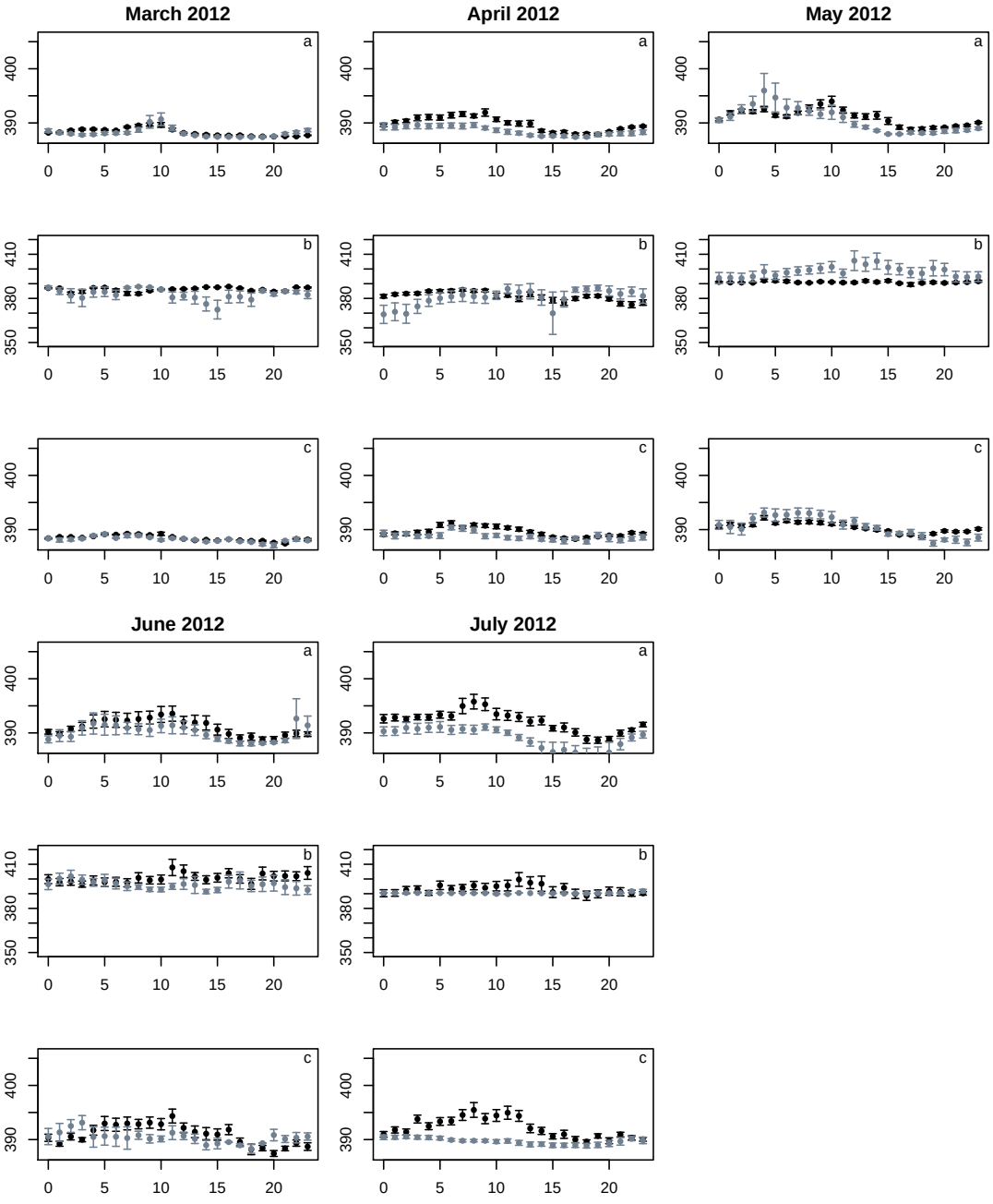
March 2012
April 2012
May 2012
June 2012
July 2012
a
b
c
390
400
350
380
410
0
5
10
15
20

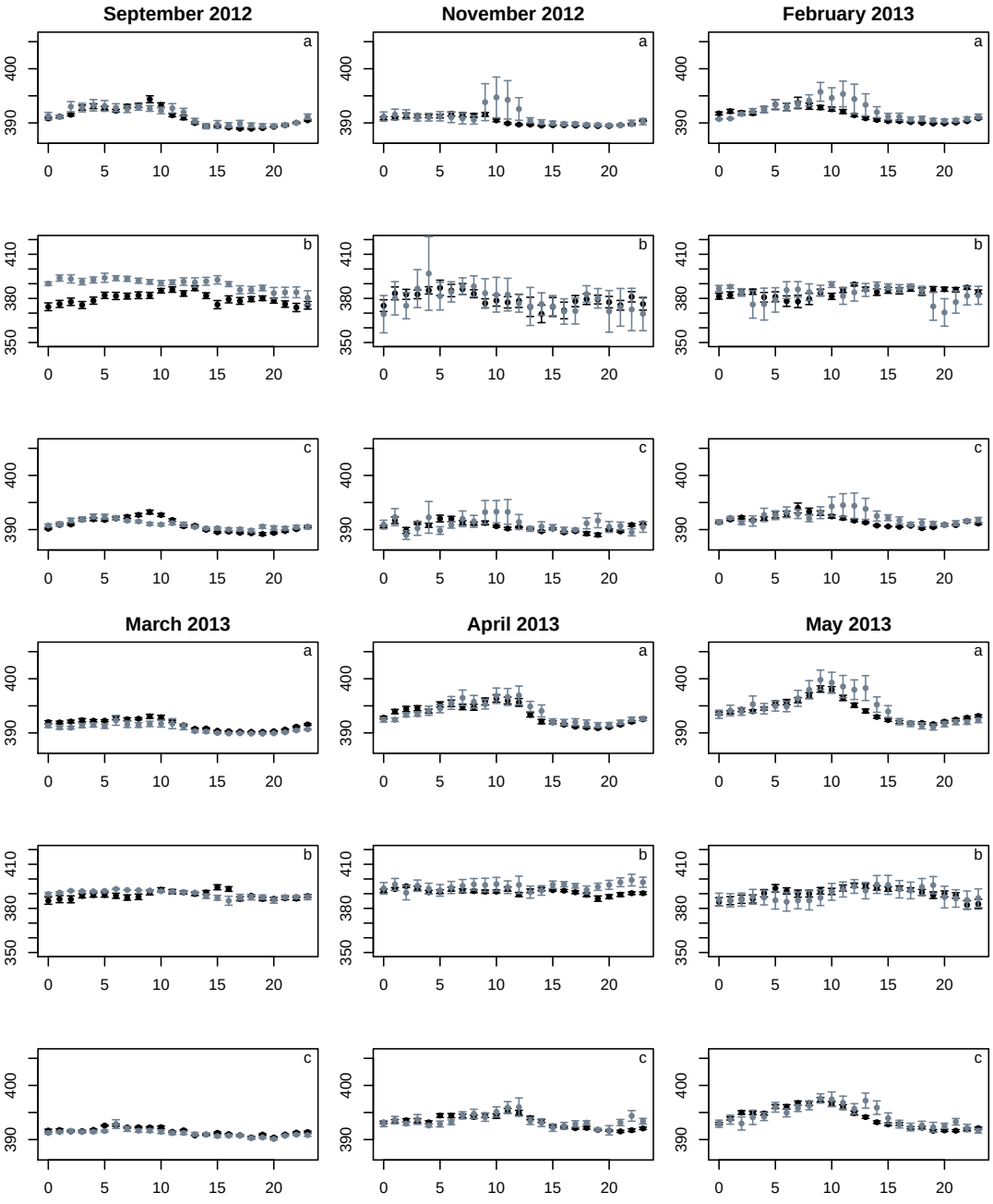
September 2012
November 2012
February 2013
March 2013
April 2013
May 2013
a
b
c
390
400
350
380
410
0
5
10
15
20

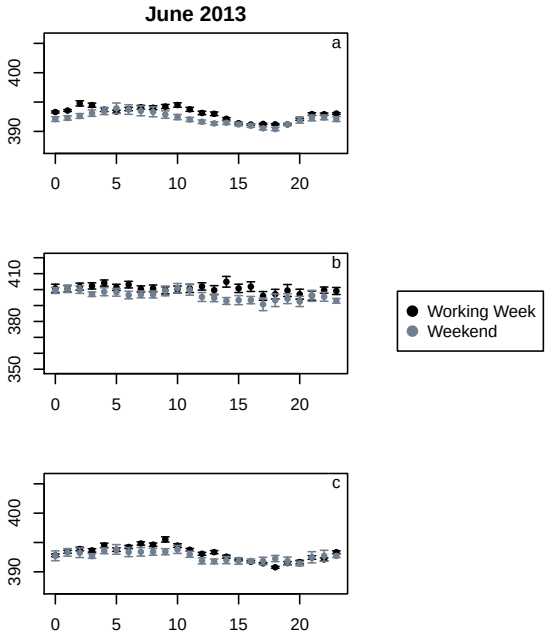

Figure 16. Diurnal cycle of the observed CO_2 concentrations (ppm) at Hangklip, separated into working week (black) and weekend concentrations (grey), for each month with standard error bars, where the standard error is calculated over all measurements available for that hour of the day during that particular month.

1.3 Weekly Flux Estimates

Section 3.2.2 provides a summary of the estimates presented here for the weekly fluxes for each month.

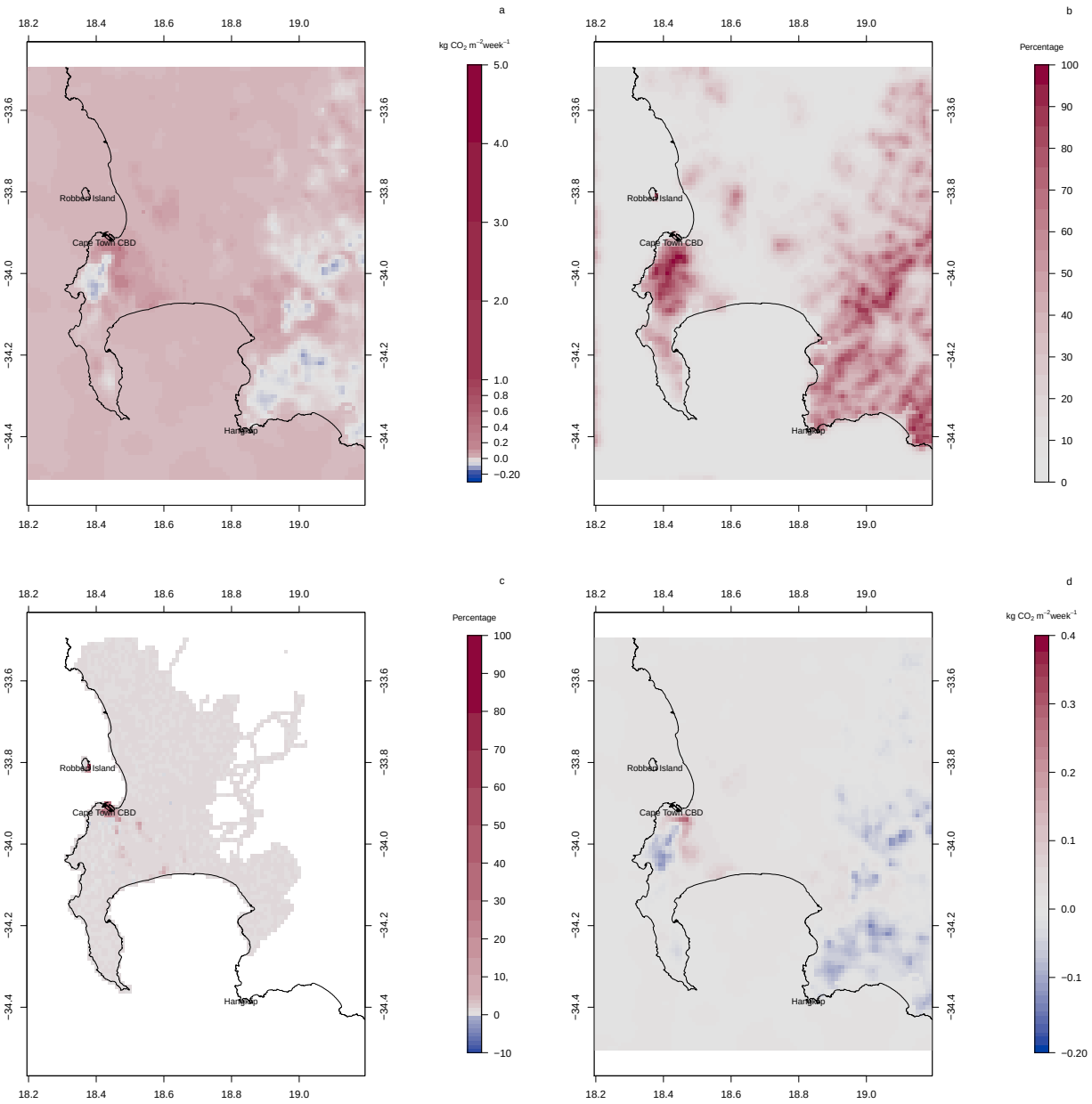

Figure 17. (a) Differences between the prior and posterior total flux estimates (kg $CO_2 m^{-2}$ $week^{-1}$) for March 2012 (prior - posterior). (b) Percentage reduction in the standard deviation of the flux estimate from prior to posterior (calculated as (1 - posterior uncertainty / prior uncertainty)×100). (c) Percentage reduction in the fossil fuel emission estimates from prior to posterior (calculated as (1 - posterior estimate / prior estimate)×100) where estimates were in kg $CO_2 m^{-2}$ $week^{-1}$. (d) Differences in the biogenic flux estimates between prior and posterior estimates (prior - posterior) (kg $CO_2 m^{-2}$ $week^{-1}$), with negative values indicating larger posterior estimates of CO_2 fluxes relative to the prior estimates. Extent: between 34.5° and 33.5° south and between 18.2° and 19.2° east.

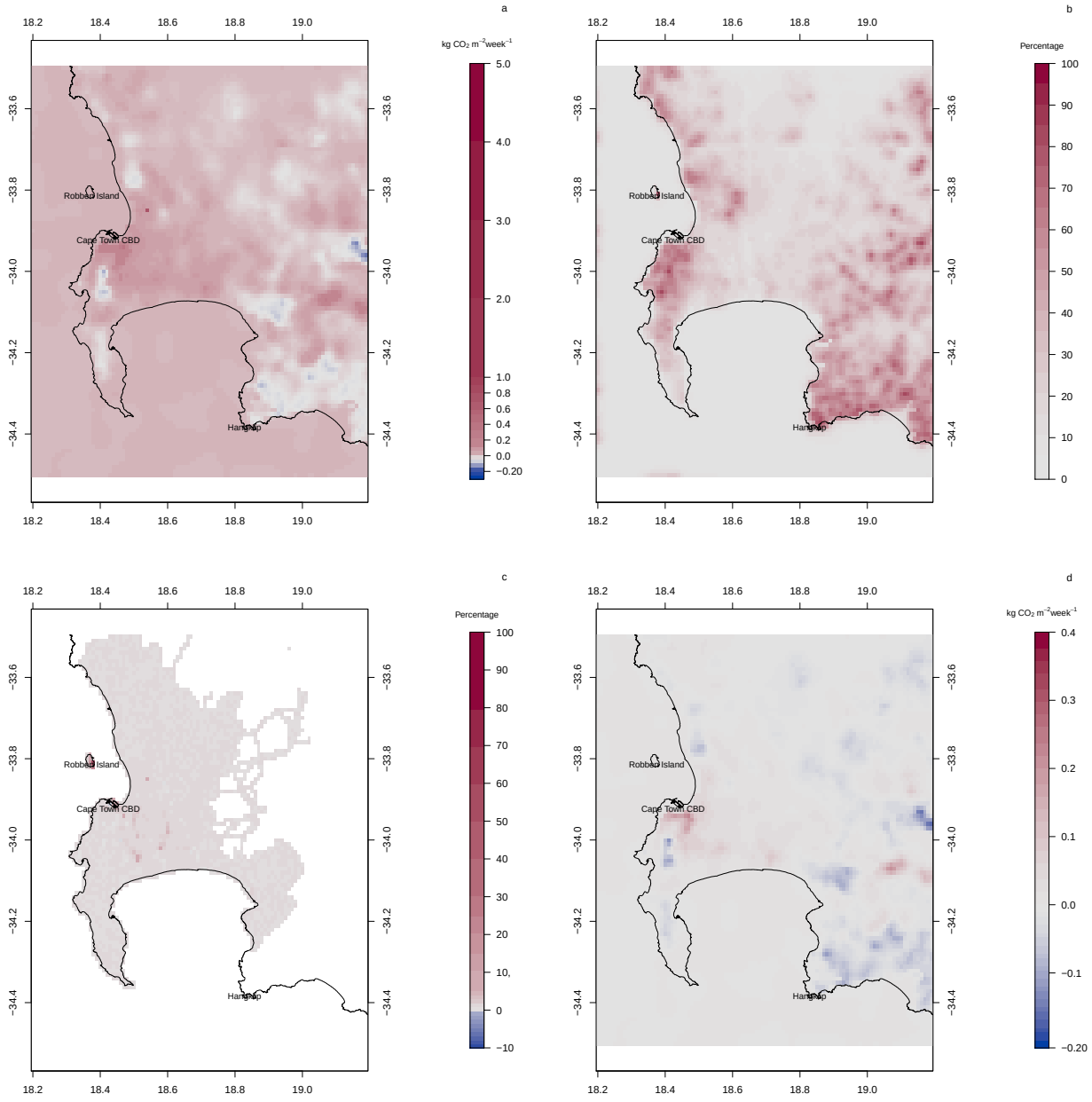

Figure 18. (a) Differences between the prior and posterior total flux estimates (kg $CO_2 m^{-2}$ $week^{-1}$) for April 2012 (prior - posterior). (b) Percentage reduction in the standard deviation of the flux estimate from prior to posterior (calculated as (1 - posterior uncertainty / prior uncertainty)×100). (c) Percentage reduction in the fossil fuel emission estimates from prior to posterior (calculated as (1 - posterior estimate / prior estimate)×100) where estimates were in kg $CO_2 m^{-2}$ $week^{-1}$. (d) Differences in the biogenic flux estimates between prior and posterior estimates (prior - posterior) (kg $CO_2 m^{-2}$ $week^{-1}$), with negative values indicating larger posterior estimates of CO_2 fluxes relative to the prior estimates. Extent: between 34.5° and 33.5° south and between 18.2° and 19.2° east.

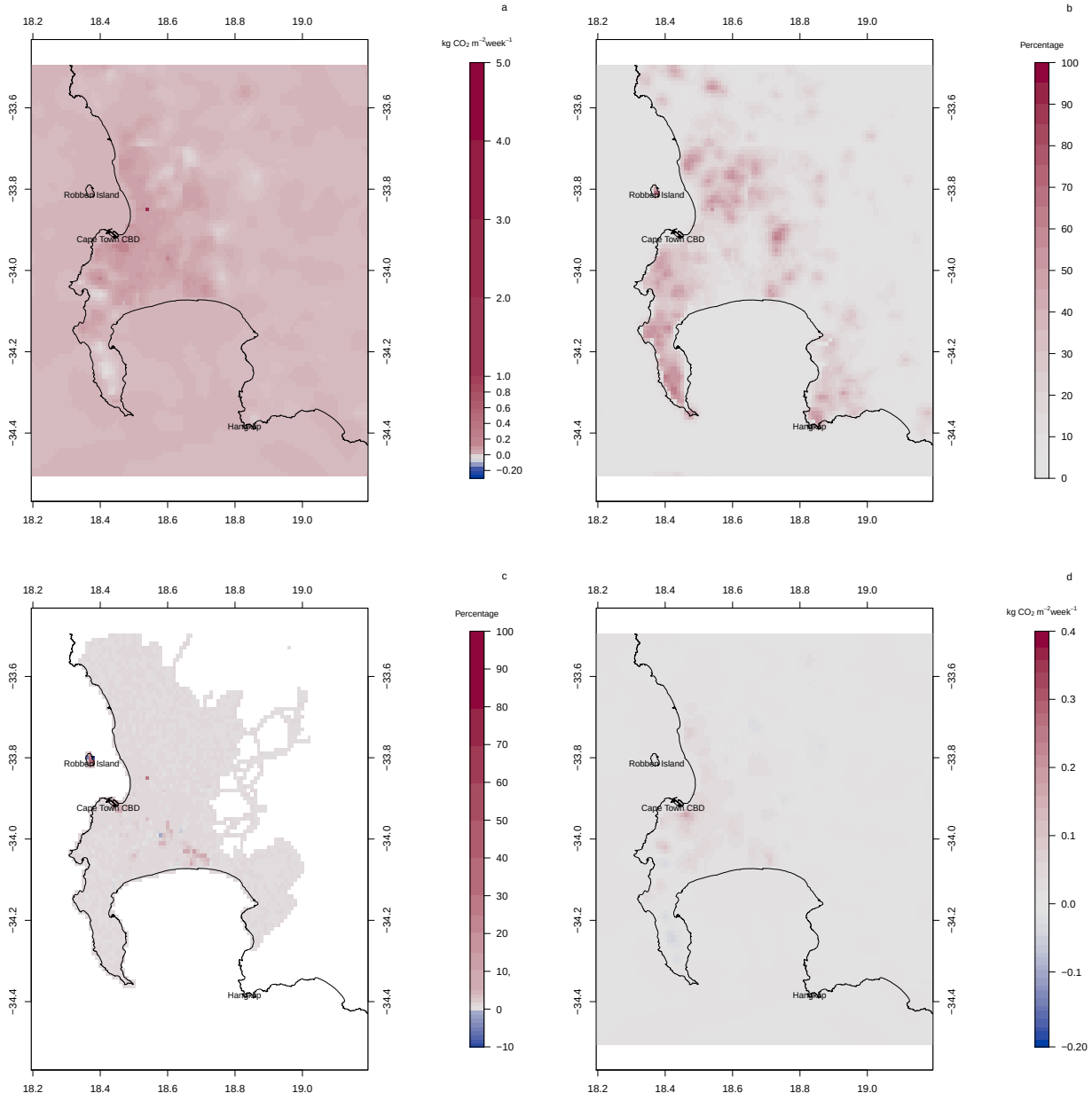

Figure 19. (a) Differences between the prior and posterior total flux estimates (kg $CO_2 m^{-2}$ $week^{-1}$) for June 2012 (prior - posterior). (b) Percentage reduction in the standard deviation of the flux estimate from prior to posterior (calculated as (1 - posterior uncertainty / prior uncertainty)×100). (c) Percentage reduction in the fossil fuel emission estimates from prior to posterior (calculated as (1 - posterior estimate / prior estimate)×100) where estimates were in kg $CO_2 m^{-2}$ $week^{-1}$. (d) Differences in the biogenic flux estimates between prior and posterior estimates (prior - posterior) (kg $CO_2 m^{-2}$ $week^{-1}$), with negative values indicating larger posterior estimates of CO_2 fluxes relative to the prior estimates. Extent: between 34.5° and 33.5° south and between 18.2° and 19.2° east.

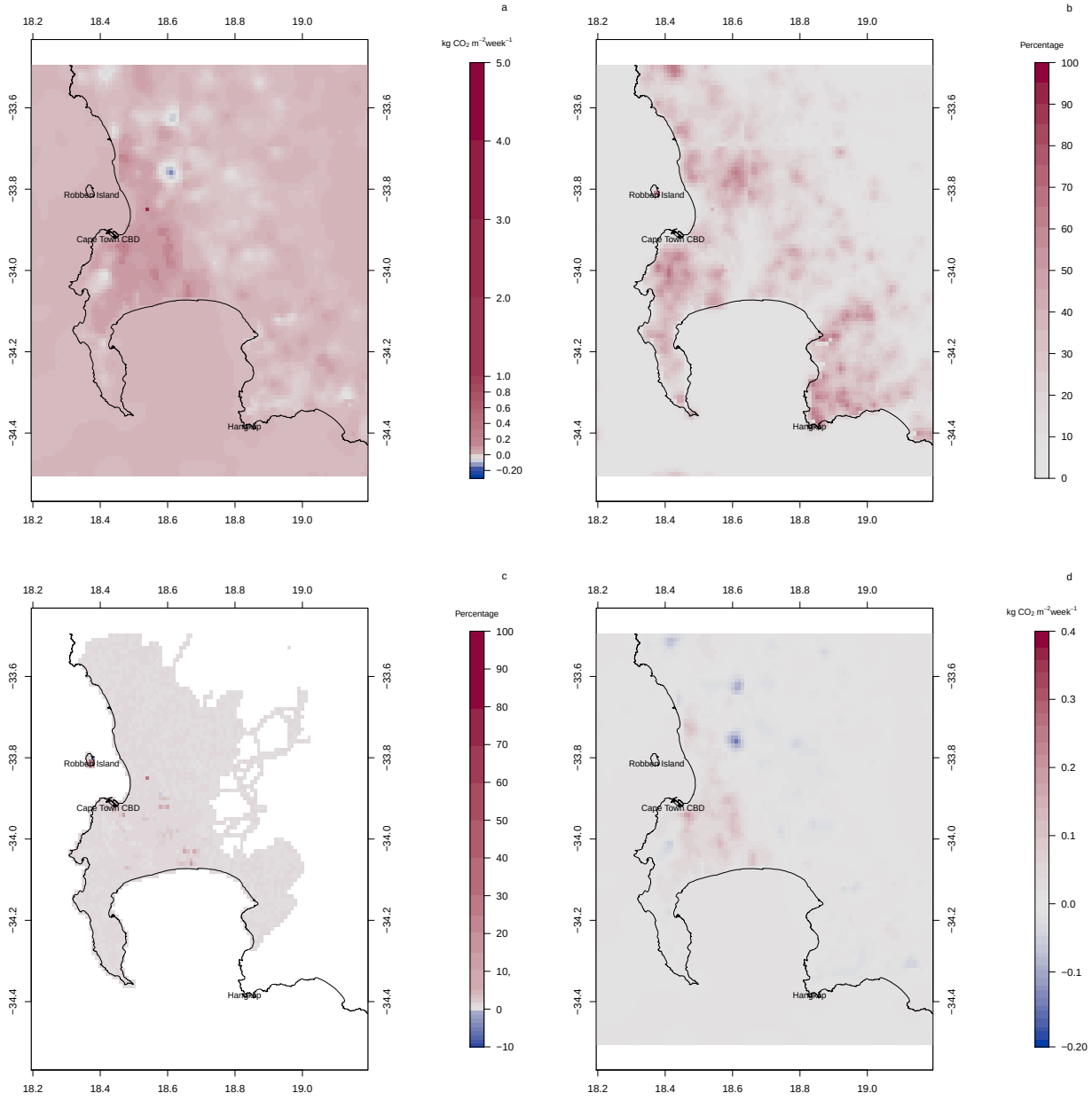

Figure 20. (a) Differences between the prior and posterior total flux estimates (kg $CO_2 m^{-2}$ $week^{-1}$) for July 2012 (prior - posterior). (b) Percentage reduction in the standard deviation of the flux estimate from prior to posterior (calculated as (1 - posterior uncertainty / prior uncertainty)$\times$100). (c) Percentage reduction in the fossil fuel emission estimates from prior to posterior (calculated as (1 - posterior estimate / prior estimate)$\times$100) where estimates were in kg $CO_2 m^{-2}$ $week^{-1}$. (d) Differences in the biogenic flux estimates between prior and posterior estimates (prior - posterior) (kg $CO_2 m^{-2}$ $week^{-1}$), with negative values indicating larger posterior estimates of CO_2 fluxes relative to the prior estimates. Extent: between 34.5° and 33.5° south and between 18.2° and 19.2° east.

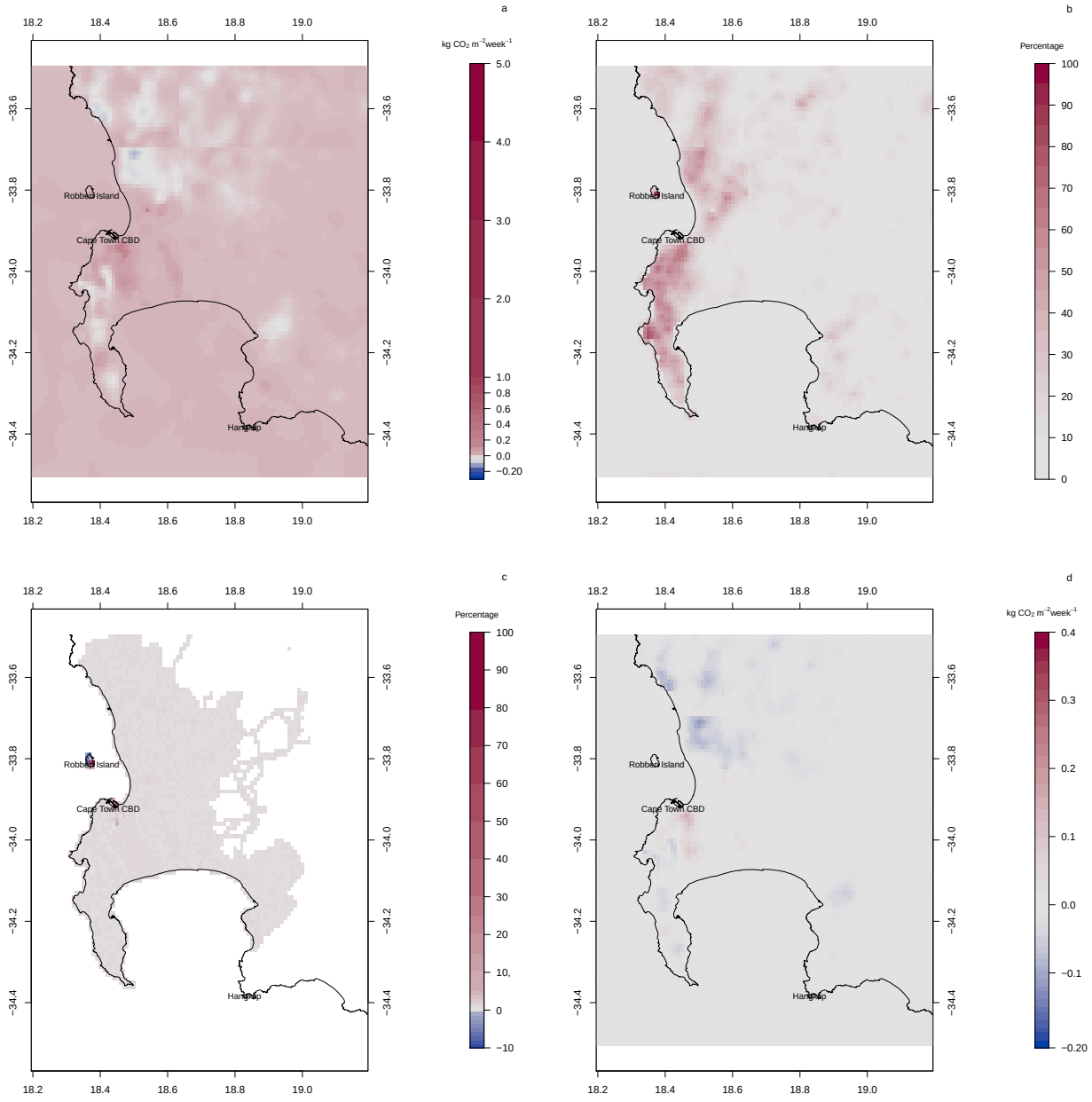

Figure 21. (a) Differences between the prior and posterior total flux estimates (kg $CO_2 m^{-2}$ $week^{-1}$) for August 2012 (prior - posterior). (b) Percentage reduction in the standard deviation of the flux estimate from prior to posterior (calculated as (1 - posterior uncertainty / prior uncertainty)×100). (c) Percentage reduction in the fossil fuel emission estimates from prior to posterior (calculated as (1 - posterior estimate / prior estimate)×100) where estimates were in kg $CO_2 m^{-2}$ $week^{-1}$. (d) Differences in the biogenic flux estimates between prior and posterior estimates (prior - posterior) (kg $CO_2 m^{-2}$ $week^{-1}$), with negative values indicating larger posterior estimates of CO_2 fluxes relative to the prior estimates. Extent: between 34.5° and 33.5° south and between 18.2° and 19.2° east.

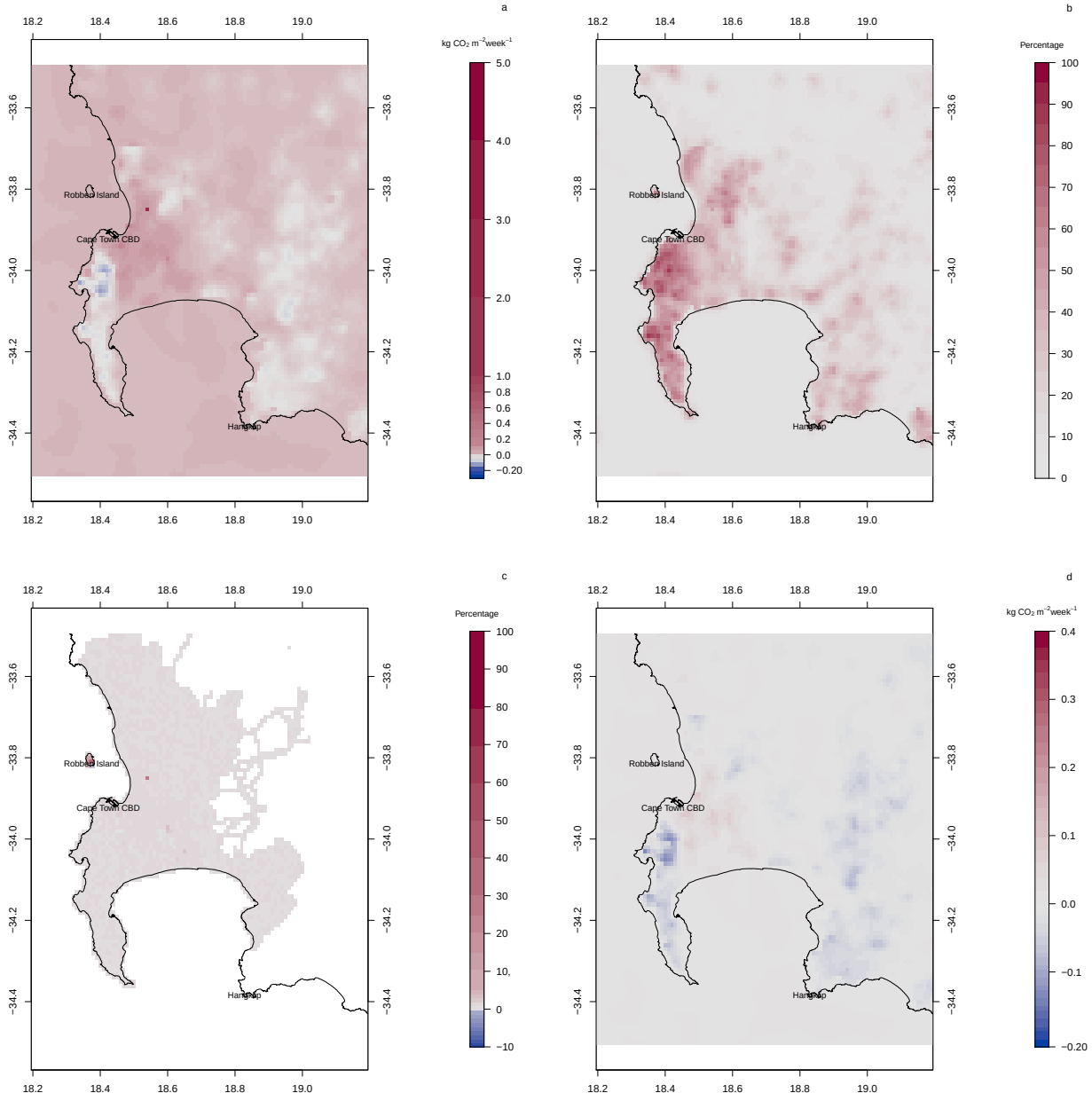

Figure 22. (a) Differences between the prior and posterior total flux estimates ($\mathrm{kg\ CO_2 m^{-2}\ week^{-1}}$) for November 2012 (prior - posterior). (b) Percentage reduction in the standard deviation of the flux estimate from prior to posterior (calculated as (1 - posterior uncertainty / prior uncertainty)$\times$100). (c) Percentage reduction in the fossil fuel emission estimates from prior to posterior (calculated as (1 - posterior estimate / prior estimate)$\times$100) where estimates were in $\mathrm{kg\ CO_2 m^{-2}\ week^{-1}}$. (d) Differences in the biogenic flux estimates between prior and posterior estimates (prior - posterior) ($\mathrm{kg\ CO_2 m^{-2}\ week^{-1}}$), with negative values indicating larger posterior estimates of CO_2 fluxes relative to the prior estimates. Extent: between $34.5°$ and $33.5°$ south and between $18.2°$ and $19.2°$ east.

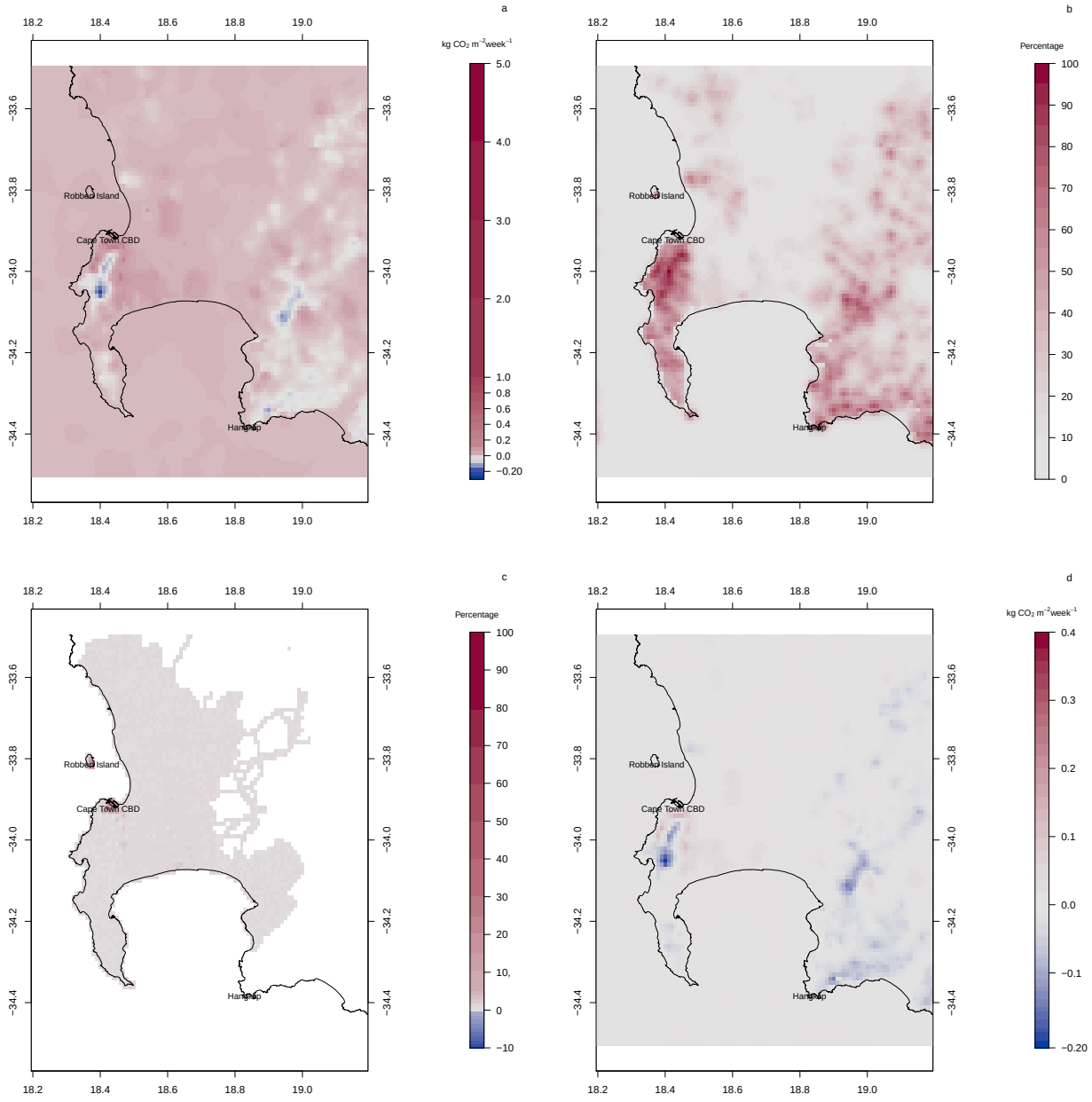

Figure 23. (a) Differences between the prior and posterior total flux estimates (kg $CO_2 m^{-2}$ $week^{-1}$) for February 2013 (prior - posterior). (b) Percentage reduction in the standard deviation of the flux estimate from prior to posterior (calculated as (1 - posterior uncertainty / prior uncertainty)×100). (c) Percentage reduction in the fossil fuel emission estimates from prior to posterior (calculated as (1 - posterior estimate / prior estimate)×100) where estimates were in kg $CO_2 m^{-2}$ $week^{-1}$. (d) Differences in the biogenic flux estimates between prior and posterior estimates (prior - posterior) (kg $CO_2 m^{-2}$ $week^{-1}$), with negative values indicating larger posterior estimates of CO_2 fluxes relative to the prior estimates. Extent: between 34.5° and 33.5° south and between 18.2° and 19.2° east.

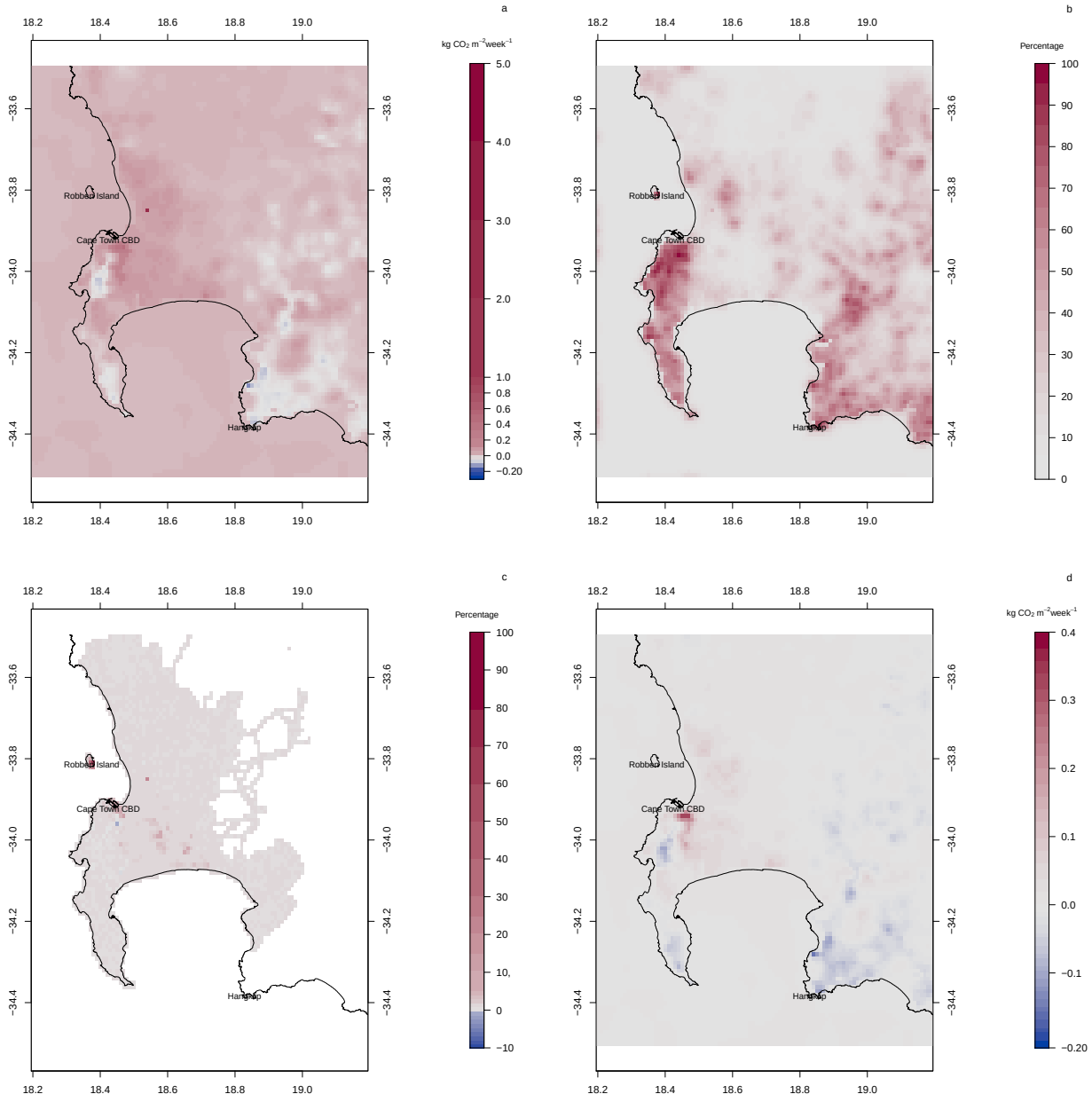

Figure 24. (a) Differences between the prior and posterior total flux estimates (kg $CO_2 m^{-2}$ $week^{-1}$) for March 2013 (prior - posterior). (b) Percentage reduction in the standard deviation of the flux estimate from prior to posterior (calculated as (1 - posterior uncertainty / prior uncertainty)×100). (c) Percentage reduction in the fossil fuel emission estimates from prior to posterior (calculated as (1 - posterior estimate / prior estimate)×100) where estimates were in kg $CO_2 m^{-2}$ $week^{-1}$. (d) Differences in the biogenic flux estimates between prior and posterior estimates (prior - posterior) (kg $CO_2 m^{-2}$ $week^{-1}$), with negative values indicating larger posterior estimates of CO_2 fluxes relative to the prior estimates. Extent: between 34.5° and 33.5° south and between 18.2° and 19.2° east.

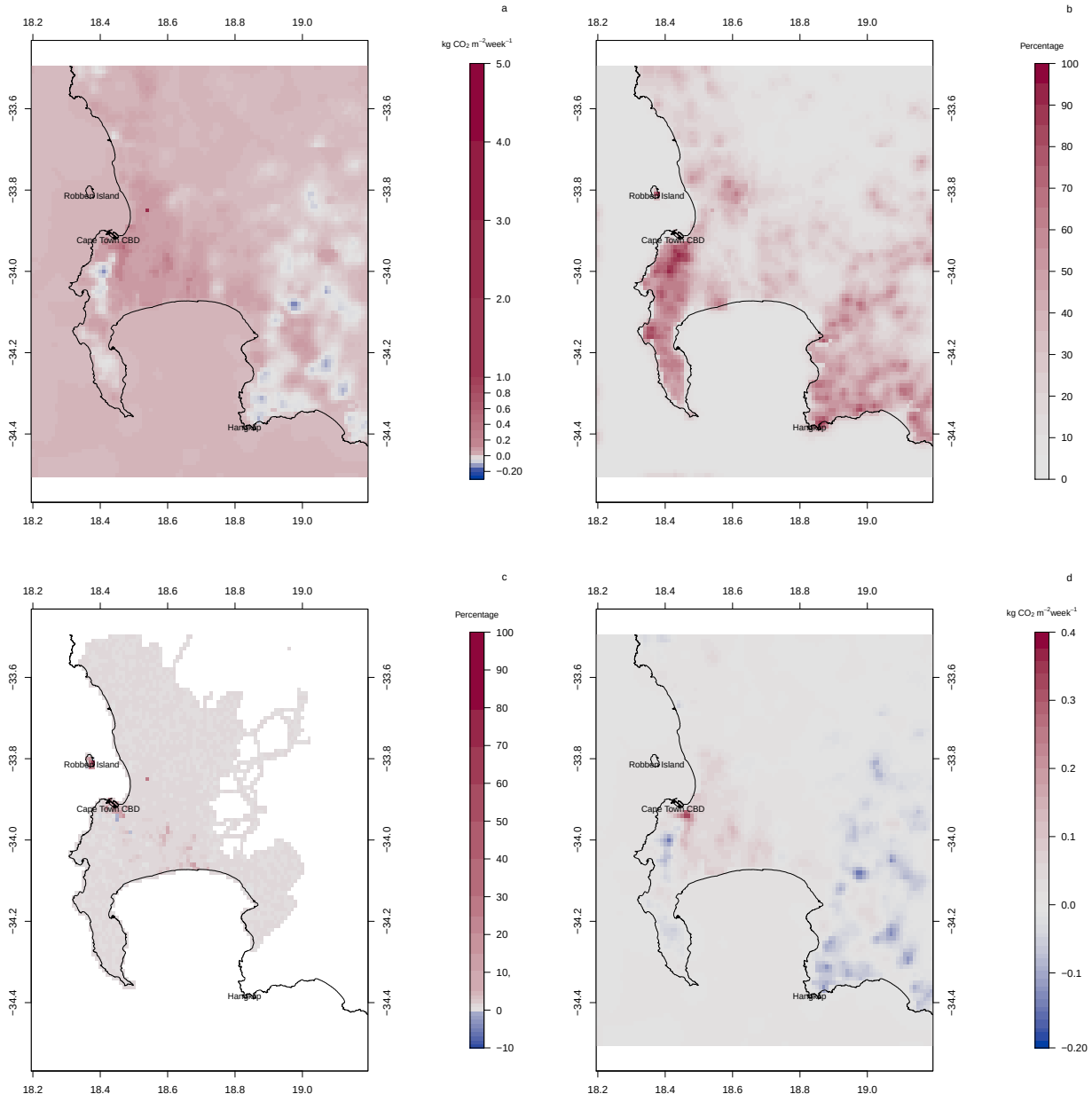

Figure 25. (a) Differences between the prior and posterior total flux estimates (kg $CO_2 m^{-2}$ $week^{-1}$) for April 2013 (prior - posterior). (b) Percentage reduction in the standard deviation of the flux estimate from prior to posterior (calculated as (1 - posterior uncertainty / prior uncertainty)×100). (c) Percentage reduction in the fossil fuel emission estimates from prior to posterior (calculated as (1 - posterior estimate / prior estimate)×100) where estimates were in kg $CO_2 m^{-2}$ $week^{-1}$. (d) Differences in the biogenic flux estimates between prior and posterior estimates (prior - posterior) (kg $CO_2 m^{-2}$ $week^{-1}$), with negative values indicating larger posterior estimates of CO_2 fluxes relative to the prior estimates. Extent: between 34.5° and 33.5° south and between 18.2° and 19.2° east.

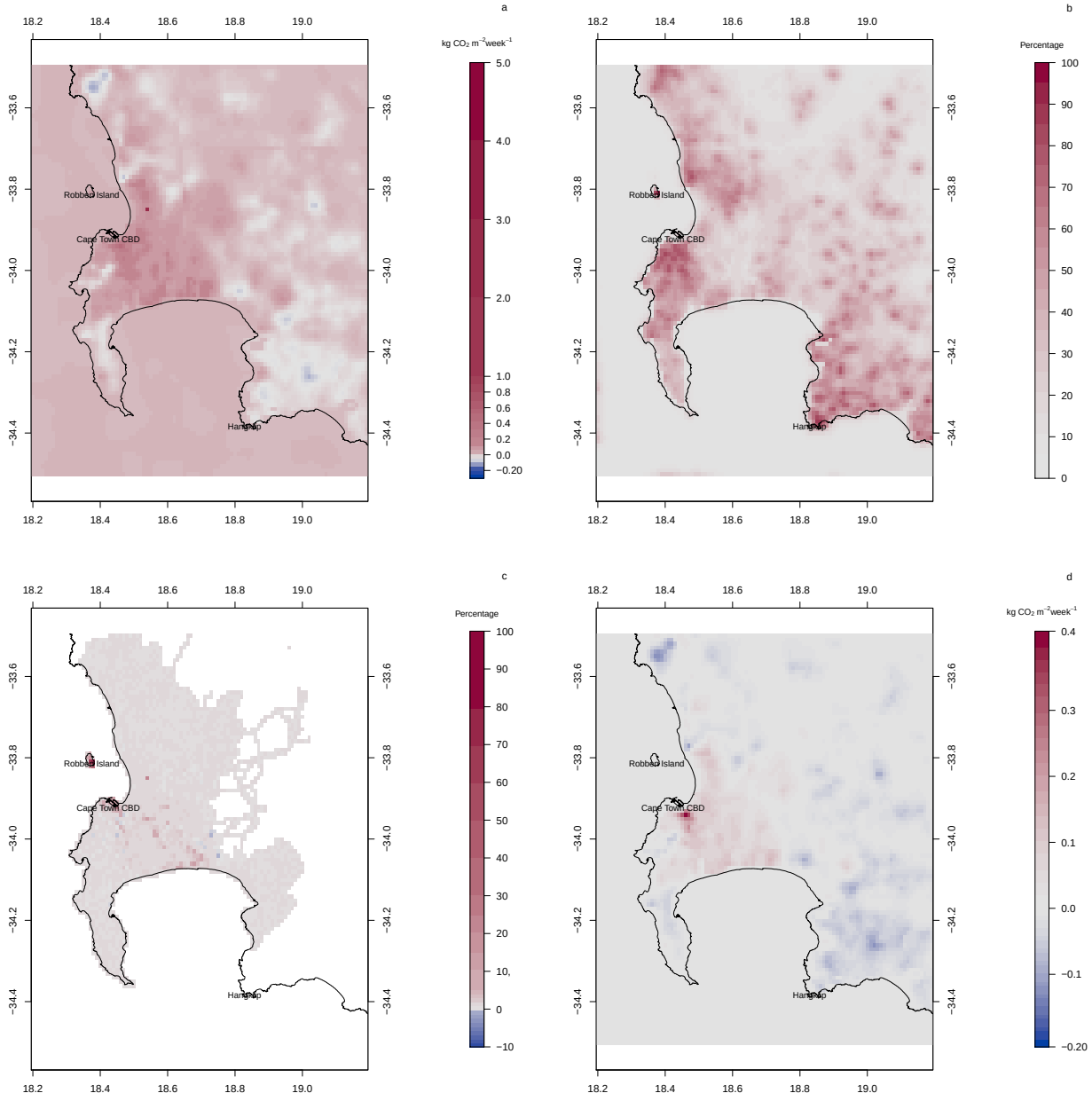

Figure 26. (a) Differences between the prior and posterior total flux estimates (kg $CO_2 m^{-2}$ $week^{-1}$) for May 2013 (prior - posterior). (b) Percentage reduction in the standard deviation of the flux estimate from prior to posterior (calculated as (1 - posterior uncertainty / prior uncertainty)×100). (c) Percentage reduction in the fossil fuel emission estimates from prior to posterior (calculated as (1 - posterior estimate / prior estimate)×100) where estimates were in kg $CO_2 m^{-2}$ $week^{-1}$. (d) Differences in the biogenic flux estimates between prior and posterior estimates (prior - posterior) (kg $CO_2 m^{-2}$ $week^{-1}$), with negative values indicating larger posterior estimates of CO_2 fluxes relative to the prior estimates. Extent: between 34.5° and 33.5° south and between 18.2° and 19.2° east.

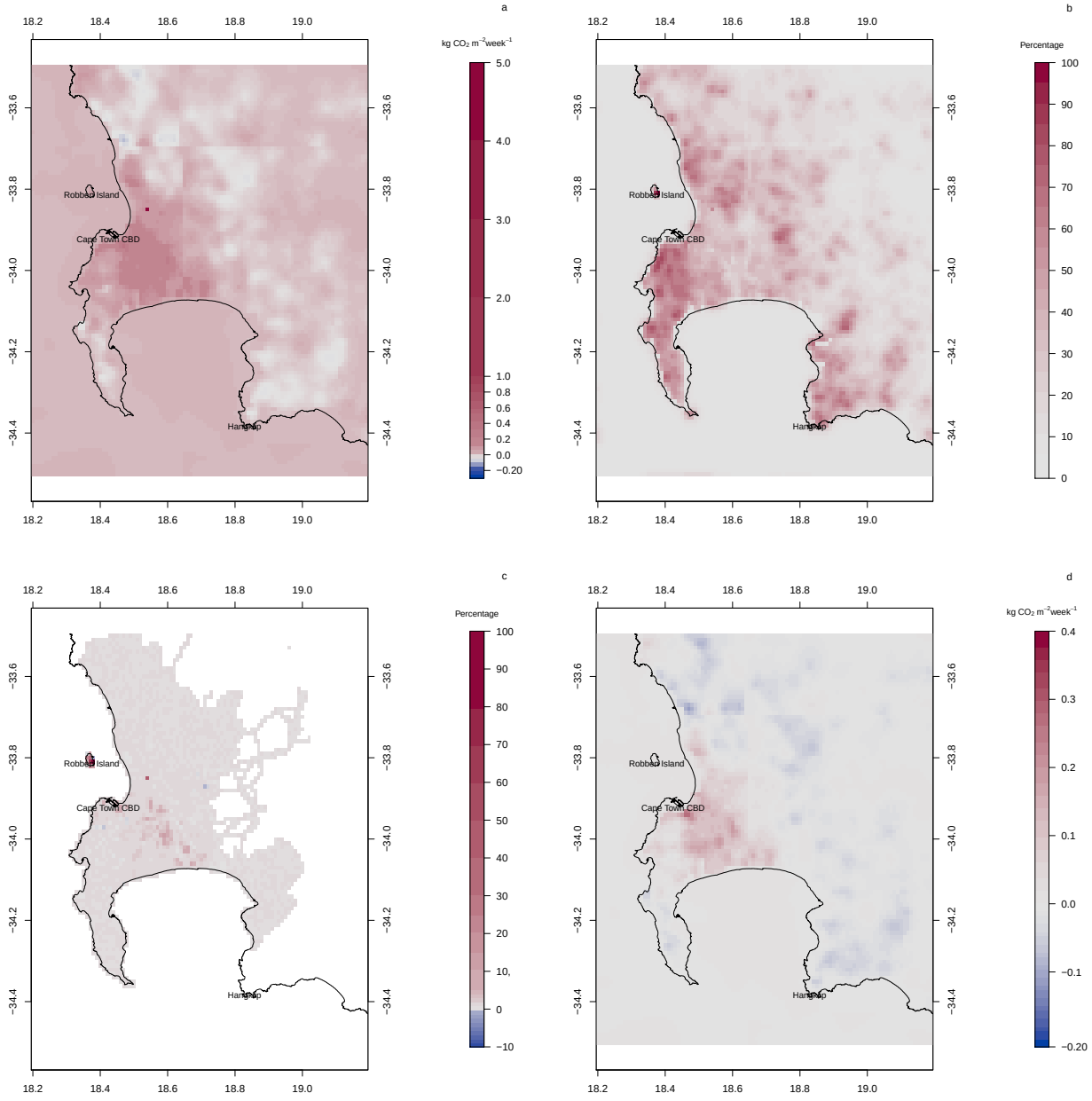

Figure 27. (a) Differences between the prior and posterior total flux estimates (kg $CO_2 m^{-2}$ $week^{-1}$) for June 2013 (prior - posterior). (b) Percentage reduction in the standard deviation of the flux estimate from prior to posterior (calculated as (1 - posterior uncertainty / prior uncertainty)×100). (c) Percentage reduction in the fossil fuel emission estimates from prior to posterior (calculated as (1 - posterior estimate / prior estimate)×100) where estimates were in kg $CO_2 m^{-2}$ $week^{-1}$. (d) Differences in the biogenic flux estimates between prior and posterior estimates (prior - posterior) (kg $CO_2 m^{-2}$ $week^{-1}$), with negative values indicating larger posterior estimates of CO_2 fluxes relative to the prior estimates. Extent: between 34.5° and 33.5° south and between 18.2° and 19.2° east.

References

Carslaw, D. C. and Ropkins, K.: openair — an R package for air quality data analysis, Environ. Model. Softw., 27–28, 52–61, doi:10.1016/j.envsoft.2011.09.008, 2012.

Engelbrecht, F. A., McGregor, J. L. and Engelbrecht, C. J.: Dynamics of the conformal-cubic atmospheric model projected climate-change signal over southern Africa, Int. J. Climatol., 29, 1013-1033., doi: 10/1002/joc.1742.29., 2009.

Engelbrecht, F. A., Landman, W. A., Engelbrecht, C. J., Landman, S., Bopane, M. M., Roux, B., McGregor, J. L., and Thatcher, M.: Multi-scale climate modelling over Southern Africa using variable-resolution global model, Water Research Commission 40-Year Celebration Conference, Kempton Park, 31 August - 1 September 2011, doi: 10.4314/wsa.v37i5.2, 2011.

Engelbrecht, C. J., Engelbrecht, F. A. and Dyson, L. L.: High-resolution model-projected changes in mid-tropospheric closed-lows and extreme rainfall events over southern Africa. Int. J. Climatol., 33, 173–187, doi: 10/1002/joc.3420, 2013

Engelbrecht, F., Adegoke, J., Bopape, M-J., Naidoo, M., Garland, R., Thatcher, M., McGregor, J., Katzfey, J., Werner, M., Ichoku, C. and Gatebe, C.: Projections of rapidly rising surface temperatures over Africa. Env. Res. Letters., 10(8), 085004, doi: 10.1088/1748-9326/10/8/085004, 2015.

Landman, S., Engelbrecht, F. A, Dyson, L., Engelbrecht, C., J., and Landman, W., A.: A short-range ensemble prediction system for South Africa, Water SA, 38(5), 765–774, doi: 10.4314/wsa.v38i5.16, 2012.

Lauvaux, T., Miles, N. L., Deng, A. Richardson, S. J., Cambaliza, M. O., Davis, K. J., Gaudet, B., Gurney, K. R., Huang, J., O'Keefe, D., Song, Y., Karion, A., Oda, T., Patarasuk, R., Razlivanov, I., Sarmiento, D., Shepson, P., Sweeney, C., Turnbull, J., and Wu, K.: High-resolution atmospheric inversion of urban CO_2 emissions during the dormant season of the Indianapolis Flux Experiment (INFLUX), J. Geophys. Res. Atmos., 121, 5213–5236, doi: 10.1002/2015JD024473, 2016.

Whittlestone, S., Kowalczyk, E., Brunke, E. G., and Labuschagne, C.: Source Regions for CO_2 at Cape Point Assessed by Modelling 222Rn and Meteorological Data, Technical Report for the South African Weather Service, Pretoria, South Africa, 2009.